Title: Metabolomic rearrangement controls the intrinsic microbial response to temperature changes

Authors: Benjamin D. Knapp[1], Lisa Willis[2], Carlos Gonzalez[3], Harsh Vashistha[4], Joanna Jammal Touma[4], Mikhail Tikhonov[5], Jeffrey Ram[6], Hanna Salman[4], Josh E. Elias[7], Kerwyn Casey Huang[1,2,7,8,†]

Affiliations:

[1]Biophysics Program, Stanford University, Stanford, CA 94305, USA

[2]Department of Bioengineering, Stanford University, Stanford, CA 94305, USA

[3]Department of Chemical and Systems Biology, Stanford University School of Medicine, Stanford, CA 94305, USA

[4]Department of Physics and Astronomy, University of Pittsburgh, Pittsburgh, PA 15260, USA

[5]Department of Physics, Washington University in St. Louis, St. Louis, MO 63130, USA

[6]Department of Physiology, Wayne State University, Detroit, MI 48201, USA

[7]Chan Zuckerberg Biohub, San Francisco, CA 94158, USA

[8]Department of Microbiology and Immunology, Stanford University School of Medicine, Stanford, CA 94305, USA

[†]To whom correspondence should be addressed: kchuang@stanford.edu

Keywords: temperature shift; Arrhenius; Michaelis-Menten kinetics; thermodynamics; entropy; enthalpy; membrane fluidity; proteomics; barcoded transposon mutant libraries; Escherichia coli; Bacillus subtilis; Schizosaccharomyces pombe; climate change

Abstract

The impact of temperature on growth is typically considered under heat- or cold-shock conditions that elicit specific regulation. In between, cellular growth rate varies according to the Arrhenius law of thermodynamics. Here, we use growth-rate dynamics during transitions between temperatures to discover how this behavior arises and what determines the temperature sensitivity of growth. Using a device that enables single-cell tracking across a wide range of temperatures, we show that bacteria exhibit a highly conserved, slow response to temperatures upshifts with a time scale of ~1.5 doublings at the higher temperature, regardless of initial/final temperature or nutrient source. We rule out transcriptional, translational, and membrane reconfiguration as potential mechanisms. Instead, we demonstrate that an autocatalytic enzyme network incorporating temperature-sensitive Michaelis-Menten kinetics recapitulates all temperature-shift dynamics, reveals that import dictates steady-state Arrhenius growth behavior, and successfully predicts alterations in the upshift response observed under simple-sugar or low-nutrient conditions or in fungi. These findings indicate that metabolome rearrangement dictates how temperature affects microbial growth.

Introduction

To proliferate and survive, microbes must integrate a vast array of environmental signals such as pH[1], salt[2], osmolarity[3], and nutrient availability[4]. All of these factors are dependent on the concentrations and identities of extracellular chemical species and are subject to intracellular regulation. By contrast, while growth is critically dependent on the environmental temperature, microbes are unable to regulate intracellular temperature. Enteric bacteria face temperature changes across time scales ranging from minutes (host colonization) to hours or days (fever), and soil and marine species are regularly exposed to daily and seasonal fluctuations. The effects of temperature can be dramatic: the largest determinant of marine bacterial community composition is local sea temperature[5], and long-term temperature changes associated with climate change are thought to substantially impact soil microbial biomass[6]. Despite these fundamental connections, the mechanistic underpinnings of how temperature affects microbial behavior remain unclear.

Most studies of how temperature affects cellular physiology have focused on the regulatory systems that enable survival under heat and cold stress, during which molecular chaperones assist in the folding and unfolding of proteins and RNA[7,8]. While growth rate decreases at extreme, stress response-inducing temperatures[9], there is typically a temperature range over which growth rate increases with temperature in agreement with the Arrhenius Law of equilibrium thermodynamics[10,11], wherein the natural logarithm of growth rate depends approximately linearly on the inverse of the absolute temperature, with a negative slope that can be interpreted as an activation

energy for growth (E_a, equivalent to the barrier for enzyme kinetics)[12]. This temperature-dependent behavior is highly conserved across diverse bacteria, archaea, yeast, and mammalian cells[12], with each species exhibiting its own Arrhenius temperature range and activation energy.

At the molecular level, enzyme catalytic rates increase with temperature until protein denaturation, with most activation energies between ~5 and 20 kcal/mol[13,14]. The evolutionary history of the highly conserved adenylate kinase suggests a trade-off between E_a and melting temperature[12,15], and theoretical work has suggested that proteome stability sets the upper bound for the growth rate of a given bacterial species. However, there is no correlation between optimal growth temperature and E_a across bacteria[10], indicating that E_a is likely influenced by factors other than proteome stability. In *Escherichia coli*, the Arrhenius range is between 23 °C and 37 °C and E_a is ~13 kcal/mol[11,16], similar to the free energy change from ATP hydrolysis (12–16 kcal/mol)[17], suggesting that there may be a single rate-limiting enzyme for growth. On the other hand, theoretical work on cyclical enzyme networks has suggested that E_a arises from the average of the activation energies over all reactions within the network[18,19]. Most central dogma processes in *E. coli* have an activation energy between 10 and 17 kcal/mol[12] and the activation energies of growth and of translation *in vivo* are virtually identical[20]. Whether the temperature sensitivity of growth depends on the details of metabolism is unclear, although previous studies reported that E_a in *E. coli* is approximately constant across some nutrient conditions[11,21]. Taken together, what is

limiting for growth across Arrhenius temperatures and what sets E_a for a given species remain unknown.

Most previous studies of growth in the Arrhenius range have focused on steady-state growth, rather than how cells respond to temperature changes. An early study of 133 proteins in *E. coli* showed that the concentration of most of these proteins was maintained across Arrhenius temperatures, suggesting that the proteome may be largely temperature insensitive[11]. However, other studies found transient changes in the synthesis of tRNA synthetases after temperature increases[22], and a decrease from 37 °C to 28 °C resulted in significant changes to ~9% of the *E. coli* transcriptome[23], perhaps reflecting the selection for coupled sensing of changes in temperature and other environmental variables such as oxygen levels relevant for animal host colonization[24]. In the few studies examining the growth rate response to temperature shifts, some report that *E. coli* growth rate responds almost immediately upon temperature shifts within the Arrhenius range[22,25], while others report much longer time scales that scale with the final temperature[21].

Many factors could determine the time scale of temperature adaptation. *E. coli* cells tightly maintain membrane fluidity across all temperatures permissible for growth by regulating membrane composition[26]. Increased membrane fluidity allows for higher respiratory metabolic rates[27], but how fluidity impacts growth rate during temperature shifts is unknown. Growth rate across nutrients correlates with ribosome concentration, which is optimized through competition between protein and autocatalytic ribosome

110 synthesis[28,29]. As a result, many models of growth focus on translation as a key growth-
111 limiting factor[30]. However, this framework is likely inappropriate for understanding
112 growth rate variations across temperatures, as ribosome concentration is constant
113 across Arrhenius temperatures[11,31].
114
115 Here, we demonstrate that *E. coli* cells exhibit an asymmetric growth-rate response to
116 temperature shifts within the Arrhenius range: during downshifts, growth-rate rapidly
117 decreases on the same time scale as that of the temperature shift, while cells gradually
118 adapt to upshifts on a time scale corresponding to ~1.5 doublings at the steady-state
119 growth rate of the final temperature, independent of nutrient source. We show that these
120 responses do not result from proteome or membrane reconfiguration or from
121 transcriptional regulation, although increased membrane fluidity was lethal at high
122 temperatures. To interrogate the mechanism underlying growth-rate adaptation to
123 temperature shifts, we developed an autocatalytic enzyme network model that
124 incorporates temperature-sensitive Michaelis-Menten kinetics into chained reactions.
125 The model quantitatively captured the asymmetric responses to up- and downshifts
126 across Arrhenius temperatures and how carbon source affects the dynamics
127 immediately after an upshift through changes in the activation energy of growth.
128 Furthermore, our model successfully predicted the larger initial acceleration and
129 decrease in upshift response time observed at sub-saturating substrate concentration
130 compared with saturation. Growth-rate dynamics during temperature upshifts were
131 highly conserved across diverse *Escherichia* strains/species and the Gram-positive
132 *Bacillus subtilis*, suggesting that certain aspects of microbial responses to temperature

shifts and hence features of the underlying metabolic network may be universally conserved. Moreover, the ability of the model to capture the distinct response of the fission yeast *Schizosaccharomyces pombe* suggests that temperature adaptation provides a window into the factors limiting growth.

137 **Results**

138

139 **The activation energy for growth in a rich growth medium is conserved across *E.***
140 ***coli* evolutionary histories**

141 To determine whether evolutionary history impacts temperature sensitivity across
142 strains of a single species, we measured the growth of 12 *E. coli* strains isolated from
143 fecal samples of hosts encompassing a broad range of body temperatures, including
144 ectothermic species such as lizards, wild mammals, household pets, humans, and birds
145 (which have body temperatures as high as 42 °C) (Table S1)[32,33]. Growth rates were
146 significantly higher in the natural isolates compared with laboratory strains (Fig. S1A),
147 which has been attributed to defects in pyrimidine biosynthesis in domesticated *E. coli*
148 strains[34,35]. Despite host body temperatures ranging between ambient and 42 °C, all
149 strains exhibited similar temperature sensitivity profiles, with Arrhenius behavior (linear
150 relationship between ln(growth rate) and 1/*T*) between 27 °C and 37 °C (Fig. S1B),
151 consistent with previous studies of *E. coli* and *Salmonella enterica* isolated from pigs,
152 squirrels, and turtles that showed little variation in temperature-dependent growth
153 rates[36]. Interestingly, the highest growth rate occurred at >37 °C for all strains,
154 regardless of the host from which it was isolated (Fig. S1A). The activation energy of
155 growth for the natural isolates varied between 8 and 14 kcal/mol (Fig. S1C), while
156 laboratory K-12 strains exhibited a slightly higher activation energy (~15 kcal/mol) (Fig.
157 S1C–E). Additionally, other laboratory *E. coli* strains (CS109, BL21) possessed
158 activation energies between 11–15 kcal/mol (Fig. S1E). These data suggest that the

159 thermodynamic properties of *E. coli* growth are conserved and that host body
160 temperature does not dictate the temperature sensitivity of enteric bacteria.
161

162 **_E. coli_ exhibits a multi-step acceleration in response to temperature upshifts**

163 To identify the mechanisms underlying the temperature sensitivity of bacterial growth,
164 we sought to capitalize on approaches that extend beyond steady-state molecular and
165 batch culture analyses. Methods such as microfluidics that enable single-cell growth-
166 rate measurements during perturbations have provided new insights into how bacteria
167 couple proteome allocation to carbon utilization and mechanical forces to growth[3,37,38].
168 Similar single-cell tracking using a microscopy-compatible temperature controller[39] can
169 be used to interrogate simple hypotheses about the molecular architecture underlying
170 temperature sensitivity. For example, if a single enzyme is rate limiting for growth, a
171 sudden temperature change should result in an immediate change in growth rate
172 consistent with the activation energy of the enzyme. By contrast, if growth rate is limited
173 by a host of enzymes or a negative feedback system, then the time scale and dynamics
174 of adaptation to a temperature shift may be more complex.
175

176 To quantify single-cell growth rates during a temperature shift, we previously designed
177 and built an inexpensive single-cell temperature controller that precisely controls sample
178 temperature during imaging[39]. Single-cell contours were used to calculate instantaneous
179 growth rate over time (Methods), measured as $\frac{1}{L}\frac{dL}{dt}$ where L is cell length[3,40]. During
180 steady-state growth, instantaneous growth rate is constant (indicating exponential
181 growth) and can be maintained for many generations[39,41]. Similar to liquid growth (Fig.

182 1A, left), single-cell growth rates of *E. coli* MG1655 displayed Arrhenius behavior (Fig.
183 S2A,B) between 25 °C and 37 °C, and cell morphology was largely maintained (Fig.
184 S2C,D) across this temperature range, in agreement with previous studies of
185 *Salmonella* Typhimirium[42]. Despite slight differences in E_a, single-cell growth rates were
186 highly correlated with those in liquid culture (Fig. 1A, inset), indicating that both methods
187 can be used to measure steady-state growth rates throughout the Arrhenius range.
188
189 For the minimal model in which growth depends only on a single enzyme whose rate
190 varies exponentially with the inverse temperature with the same activation energy as
191 growth, instantaneous growth rate would adapt immediately to the steady-state value
192 dictated by the current temperature. Hence, the time scale of growth-rate adaptation
193 would match that of a temperature shift (for our device, ~1 min). Similar behavior is
194 predicted for a model in which all reactions important for growth have the same
195 temperature dependence. To test whether such a minimal model applies to *E. coli*, we
196 monitored the growth of single cells on LB agarose pads during 10 °C temperature
197 shifts within the Arrhenius range (27 °C and 37 °C). A rapid downshift from 37 °C to
198 27 °C resulted in a rapid decrease in growth rate with a timescale quantitatively similar
199 to that of temperature (Fig. 1B), nearly reaching the steady-state growth rate at 27 °C,
200 and then slowly decelerating toward the new steady state (Fig. 1B). Growth rate
201 dynamics closely followed those of temperature across a range of downshifts (Fig. S3).
202
203 By contrast, temperature upshifts from 27 °C to 37 °C resulted in a slow and
204 qualitatively distinct response from downshifts, with an initial “spike” that peaked at ~3

min post-shift and subsequent linear acceleration until reaching the 37 °C steady-state growth rate at ~40 min post-shift (Fig. 1C), a response time (Methods) substantially longer than the doubling time at 37 °C (~22 min). This behavior indicates that the minimal model is not generally applicable, and that some aspect of growth cannot immediately respond as temperature increases.

The response time to a temperature upshift is determined by the steady-state doubling time at the higher temperature

To identify factors that affect the response time to temperature upshifts, we shifted *E. coli* from steady-state growth on LB at 27 °C to 30 °C, 33 °C, or 37 °C and monitored the instantaneous growth rate dynamics of single cells. In each case, the upshift caused an initial spike and subsequent linear acceleration up to the steady-state growth rate at 37 °C (Fig. 1C,D). However, the time scale of the overall response depended on the final temperature. When cells were shifted to 33 °C, the response time was longer than after an upshift to 37 °C, despite the smaller difference in steady-state growth rate between the initial and final temperature, and the response time for the shift to 30 °C was even longer (~60 min, Fig. 1D).

To test whether the response is largely determined by the increased growth rate at the elevated final temperature, we transformed our measurements of growth-rate dynamics, normalizing time t by the doubling time at the final temperature (τ_D) to obtain the thermal time t/τ_D (Fig. 1E). After normalizing the change in growth rate by the difference in steady-state growth rate at the initial and final temperature, we found that

228 all trajectories collapsed (at least within the noise of our measurements) onto a single
229 curve, with response time of 1.6±0.2 doublings at the final temperature (Fig. 1F,
230 Methods). The same collapse was observed for a broad range of temperature upshifts
231 within the Arrhenius range between steady-state growth rates spanning 0.6 h^{-1} to 2.0 h^{-1}
232 (Fig. 1F), suggesting a highly conserved behavior.
233
234 While these findings suggest that the response time depends entirely on the growth rate
235 at the final temperature, growth rate and temperature are inherently coupled by the
236 Arrhenius behavior (Fig. 1A, S1B,E). To uncouple the effects of growth from
237 temperature, we performed temperature shifts of *E. coli* on LB from 27 °C to 40 °C or
238 42 °C, temperatures at which the growth rate is nearly identical to that at 37 °C (Fig.
239 S4A)[16]. An upshift to 40 °C resulted in a spike similar to the upshift to 37 °C, followed
240 immediately by a deceleration back to the 27 °C growth rate (Fig. S4A) that was likely
241 due to heat-shock pathway activation. Cells then accelerated to the 40 °C steady-state
242 growth rate within 35 min, similar to the upshift to 37 °C, corresponding to a response
243 time of ~1.4 doublings (Fig. S4B). Similar behavior was observed after an upshift to
244 42 °C (Fig. S4A,B). These data provide further evidence that the response time is set by
245 growth kinetics at the final temperature.
246
247 To determine whether the response to a temperature upshift is specific to LB, we
248 monitored *E. coli* cells during an upshift from 27 °C to 37 °C while growing on minimal
249 media supplemented with glucose or glycerol (Fig. 1G). Each normalized growth
250 trajectory was highly similar to that observed on LB, with a response time of 1.3–1.6

251 doublings (Fig. 1H); the main difference was the absence of an initial spike (Fig. 1G,H).
252 The rapid growth rate of *E. coli* on LB is due mainly to the presence of amino acids[43],
253 and growth on minimal medium supplemented with casamino acids or on glucose
254 supplemented with L-glutamate produced an initial spike and a response time of 1.3–1.5
255 doublings (Fig. 1G,H). Thus, the response time is conserved across many growth
256 media.
257

258 **Temperature upshift responses are unaffected by oxygen or chaperones**

259 We initially considered the possibility that the delayed response after an upshift is
260 regulated by the induction of a stress response at a rate set by the doubling time at the
261 final temperature. For example, an increase from room temperature to 37 °C induces
262 transcriptional responses associated with oxygen starvation[24]. Moreover, molecular
263 chaperones account for ~3% of the proteome at 37 °C, suggesting that folding
264 assistance is important even within the Arrhenius temperature range[16].
265

266 To examine the role of oxygen in temperature upshift responses, we subjected MG1655
267 cells to an upshift from 25 °C to 37 °C on LB under anaerobic conditions (Methods).
268 Normalized response dynamics were virtually identical to those during an aerobic
269 temperature upshift, even though the steady-state growth rate at 37 °C was slightly
270 lower in anaerobic (~1.8 h^{-1}) versus aerobic (~2 h^{-1}) conditions (Fig. S5A,B). Thus, the
271 presence of oxygen likely has no impact on temperature upshift responses.
272

273 The major heat-shock chaperone DnaK increases ~2-fold in concentration between 37 °C
274 and 42 °C[16], and Δ*dnaK* cells exhibited substantial growth defects when shifted from
275 37 °C to 42 °C compared with wild type (Fig. S5C). To quantify the role of heat stress in
276 upshift responses, we subjected Δ*dnaK* cells to a temperature upshift from 27 °C to 37 °C
277 on LB. Despite having a slightly lower steady-state growth rate (1.8 h^{-1}, Fig. S5D) at 37 °C
278 compared with wild type, in addition to a deceleration after the initial spike (Fig. S5D), the
279 normalized response time of Δ*dnaK* cells was nearly identical (~1.7 doublings) (Fig. S5E).
280
281 Under nutrient limitation, the enzymes SpoT and RelA produce the alarmone ppGpp,
282 which signals large-scale transcriptional reprogramming known as the stringent
283 response that regulates metabolism[44,45]. Temperature increases from the Arrhenius
284 range (23 °C–37 °C) to 40 °C or 42 °C in *E. coli* result in a transient increase in
285 ppGpp[22,46]. To determine whether the stringent response is responsible for the growth
286 delay during upshifts, we investigated the behavior of a Δ*spoT* Δ*relA* mutant deficient in
287 ppGpp production[47] (Methods). The double mutant exhibited slight steady-state growth
288 defects at 27 °C and 37 °C on LB (Fig. S5F). During an upshift from 27 °C to 37 °C, the
289 double mutant displayed an initial spike similar to wild type, followed by deceleration
290 back to the steady-state growth rate at 27 °C (Fig. S5F). Cells then accelerated to their
291 steady-state growth rate at 37 °C with a response time of ~2.3 doublings (Fig. S5G),
292 somewhat higher than the response time for the parent strain (~1.8 doublings) (Fig.
293 S5G). During a shift from 27 °C to 42 °C, Δ*spoT* Δ*relA* cells exhibited a very small spike
294 followed by rapid deceleration from 0.8 h^{-1} to 0.4 h^{-1} (Fig. S5H), consistent with the
295 transient increase in ppGpp previously observed in these conditions[22,46]. Thus, the

296 stringent response is important for growth at heat-shock temperatures, and its impact on
297 the growth response to upshifts suggests that the response time scale is related to
298 metabolism.
299

300 **Rapid growth-rate adaptation to high temperature shocks**

301 How *E. coli* growth rate responds on short time scales to heat shock is surprisingly
302 unknown, despite the abundance of knowledge on regulatory responses[48-51]. To
303 examine this regime, we monitored the growth of single MG1655 cells during an upshift
304 from steady-state growth at 37 °C to 40 °C, 42 °C, 43 °C, or 47 °C. An upshift to 40 °C
305 resulted in an initial ~20% decrease in growth rate, followed by a rapid acceleration after
306 ~13 min back to the steady-state growth rate at 37 °C (Fig. S6A). An upshift to 42 °C
307 resulted in a larger growth rate decrease (30%), and cells required longer (~20 min) to
308 recover back to ~90% of the 37 °C steady-state growth rate (Fig. S6A). At 43 °C, the
309 growth rate decreased by ~40%, then accelerated to an intermediate growth rate (1.6 h^{-}
310 ^{1}) after 25 min (Fig. S6A). An upshift to 47 °C resulted in rapid deceleration from 2 h^{-1} to
311 0.5 h^{-1}, without any subsequent acceleration (Fig. S6A). Nonetheless, cells exposed to
312 short (5 min) or long (36 min) pulses at 47 °C were able to recover back to the 37 °C
313 steady-state growth rate within 5 and 45 min, respectively (Fig. S6B), indicating that
314 temperature stress is cumulative and *E. coli* growth is robust to high-temperature
315 fluctuations.
316

317 ***E. coli* quickly resumes rapid growth after a cold-shock pulse**

318 Whereas the heat-shock response primarily deals with protein destabilization and
319 unfolding, the cold-shock response induces expression of a suite of chaperones that
320 stabilize RNA[7]. Instantaneous growth-rate responses immediately after low temperature
321 exposure are virtually unknown. Thus, we subjected MG1655 cells growing at 37 °C on
322 LB to cold pulses at 18 °C, 12 °C, and 0 °C (Fig. S6C–F, Methods). Similar to
323 downshifts within the Arrhenius range, growth rate decreased rapidly upon the
324 temperature downshift (Fig. S6C,E). At 18 °C, cells then quickly accelerated from ~0.2
325 h^{-1} to ~0.4 h^{-1} and remained at that growth rate until the upshift back to 37 °C (Fig.
326 S6C). At 12 °C, growth rate initially decreased to ~0 h^{-1}, followed by steady acceleration
327 to ~0.2 h^{-1} until the upshift back to 37 °C (Fig. S6C). When shifted down to 0 °C (Fig.
328 S6D–F), cells shrank in size, represented by deceleration to a negative growth rate (-1.3
329 h^{-1}), followed by acceleration to 0 h^{-1} (Fig. S6E). During the upshifts back to 37 °C, there
330 was a large initial spike followed by linear acceleration back to the steady-state growth
331 rate at 37 °C over 20 min (Fig. S6E), all without any cell death (Fig. S6F). Thus, *E. coli*
332 can quickly respond to cold shock pulses and robustly and rapidly exit cold shock.
333

334 **Downshift pulses reveal dependence on temperature history**

335 Since the response to a downshift occurs within minutes, whereas adaptation to an
336 upshift requires longer than the doubling time at the final temperature, it is likely that a
337 component(s) limiting for growth must be produced to attain the steady-state growth
338 rate at the higher temperature. In the absence of rapid degradation, after a temperature
339 downshift the level of such a limiting component would represent memory of the growth

340 state at the higher temperature until it is slowly diluted by growth down to its steady-
341 state value at the lower temperature.
342
343 To evaluate this hypothesis, we monitored MG1655 cells during temperature downshift
344 pulses from 37 °C to 25 °C and back to 37 °C of varying duration. As we hypothesized,
345 after a short (10 min) interval at 25 °C, instantaneous growth rate quickly (within <10
346 min) recovered back to the 37 °C steady state (Fig. 1I), accompanied by a larger spike
347 than for cells starting from steady-state growth at 25 °C (Fig. 1I). For the longest interval
348 at 25 °C (30 min), the response time after the upshift back to 37 °C was still faster (~25
349 min, Fig. 1I) than the steady-state response (~40 min), indicating that cells did not fully
350 equilibrate to 25 °C 30 min after a downshift from 37 °C, even though growth rate had
351 largely stabilized. Similar dynamics were observed in downshift pulses from 37 °C to
352 27 °C (Fig. S7A). Furthermore, cells shifted back to an intermediate temperature (30°C
353 rather than 37 °C) after 5 min at 23 °C were able to reach the new steady-state growth
354 rate almost immediately (Fig. S7B). These results suggest that a growth-limiting
355 component is slowly diluted at the lower temperature, as cells can respond quickly to
356 temperature fluctuations.
357
358 **The *E. coli* proteome is mostly invariant across temperatures in the Arrhenius**
359 **range**
360 The standard view of growth rate modulation by nutrients is that changes in growth rate
361 are accompanied by proteome reallocation, whereby certain functional groups of
362 proteins such as ribosomes shift in relative abundance to optimize growth on the

363 provided substrates[52]. The prevailing model for growth optimization is that growth rate
364 and ribosome concentration are directly coupled[30,53,54], due to the limitation that
365 ribosomes must produce themselves in addition to all other proteins[28,55]. Therefore, we
366 considered the possibility that the response time to temperature upshifts is determined
367 by reallocation of the proteome sectors important for growth. Within this picture, the
368 rapid response to downshifts and the history dependence of growth rate during
369 downshift pulses might be due to proteins limiting for growth at higher temperatures
370 being overly abundant during the downshift.
371
372 To test this hypothesis, we performed untargeted proteomics on *E. coli* MG1655 during
373 steady-state growth on three media (LB or minimal media supplemented with glucose or
374 glycerol) at 25 °C, 30 °C, and 37 °C. Temperatures outside of the Arrhenius range
375 (16 °C, 43 °C) were also assayed in LB as positive controls for temperature stress-
376 response pathways. Proteins from two biological replicates for each condition were
377 extracted and subjected to liquid chromatography tandem mass-spectrometry (LC-
378 MS/MS, Methods). Of the 4,285 known open reading frames in the *E. coli* MG1655
379 genome, 1,918 (44.8%) proteins were identified in each of the 22 samples, similar to the
380 proteome recovery rate of previous studies[56], accounting for ~91% of the total proteome
381 estimated from ribosomal profiling (Fig. S8A)[57]. Replicates were highly correlated for all
382 conditions (r=0.96–1.0) (Fig. S8B,C).
383
384 We annotated each protein utilizing the Clusters of Orthologous Groups (COG)
385 database[58], which we modified to 9 groups to include ribosomal proteins and remove

386 non-bacterial functions (Fig. 2A; Methods). As expected, at 37 °C the ribosomal protein
387 fraction was positively correlated with the growth rate in each medium (Fig. 2B, light
388 blue), while the protein fraction associated with energy and metabolism was negatively
389 correlated with growth rate in each medium (Fig. 2C, light blue). However, the fraction
390 associated with each functional group was virtually constant across Arrhenius
391 temperatures in all three media (Fig. 2D,E, S8D), including proteome fractions of each
392 ribosomal subunit (Fig. S8E). We only observed significant changes for temperatures
393 outside the Arrhenius range that were consistent with known stress-response pathways
394 (Fig. S8D,F,G)[16]. Thus, ribosome fraction is unlikely to drive growth rate changes across
395 temperatures.
396
397 The relative abundance of most individual proteins did not change significantly across
398 temperatures. Only 13 proteins exhibited a >2-fold change between 25 °C and 37 °C
399 independent of growth medium (Fig. S9). The protein exhibiting the largest change was
400 the DNA-binding StpA, which increased 14-fold between 25 °C and 37 °C during growth
401 in minimal medium with glucose (Fig. S9A). Nonetheless, Δ*stpA* cells exhibited a similar
402 response to a temperature upshift from 25 °C to 37 °C on LB as wild-type cells (Fig.
403 2F,G), as did individual knockouts of the three next most temperature-dependent
404 proteins (Fig. 2F,G), regardless of whether the temperature dependence of their
405 abundance was positive or negative (Fig. S9). Thus, the *E. coli* proteome is largely
406 insensitive to temperature at steady state, and proteins with the largest abundance
407 changes across Arrhenius temperatures do not impact the growth-rate response to
408 temperature upshifts.

409

410 **Transposon mutant library screening did not identify any genes associated with**
411 **temperature upshifts**

412 We next sought to identify genes that affect the response to temperature shifts. We
413 performed a genome-wide screen using a pooled, randomly barcoded transposon
414 mutant library in *E. coli* BW25113. This library consists of ~150,000 unique mutants,
415 each with a 20-nt DNA barcode inserted randomly into the genome near the
416 transposon[59]. By amplifying and sequencing the 20-nt barcodes, the relative abundance
417 of each mutant can be quantified in high throughput. We grew the library overnight
418 under selection at 37 °C in LB, passaged it in fresh LB at 25 °C or 37 °C until growth
419 reached a steady state, and then shifted to 37 °C or 25 °C for 90 min, respectively (Fig.
420 3A) (Methods). As controls, we also maintained cultures in steady state at 25 °C or
421 37 °C for 90 min. Cells were sampled 15 min before, at the time of, and 10, 20, 30, 40,
422 60, and 90 min after the upshift (Fig. 3A). The sample reached the target temperature
423 within 5 min (Fig. S10A) and optical density was measured at each sampling time point
424 (Fig. S10B).

425

426 No gene disruptions were consistently identified across biological replicates with a
427 significant fitness defect specific to the temperature upshift (Fig. 3B,C, S10C).
428 Disruption of four genes (*trmE*, *lon, ndk, yciO*) was deleterious in the upshift experiment
429 (Fig. 3B), but also in the 25 °C controls (Fig. 3C). Deletion of the genes that were most
430 deleterious across upshift replicates (*lon, clpP, lepA*) (Fig. 3B,C, S10C) resulted in
431 growth defects at the single-cell level (Fig. S10D), but the normalized response time to

432 an upshift was virtually identical to wild type (Fig. S10E). Disruption of four genes
433 resulted in a fitness defect during the downshift, but not consistently across replicates
434 (Fig. S10F). Additionally, none of these gene disruptions displayed a monotonic
435 decrease in fitness after the downshift (Fig. S10F), suggesting that no non-essential
436 genes are required for downshift adaptation.
437
438 While screening of temperature shifts did not uncover any genes of interest, we
439 reasoned that the initial passaging at 25 °C to reach steady-state growth may have
440 resulted in the extinction of mutants with growth defects at low temperatures. Therefore,
441 we compared the relative abundance of each mutant between steady-state growth at
442 25 °C and 37 °C. The only gene for which disruption was deleterious at 25 °C in both
443 biological replicates was *uup* (Fig. 3D, S10G). Uup belongs to the ATP-binding cassette
444 (ABC) protein ABC-F family and has been suggested to directly bind ribosomes and
445 assist in their assembly[60]. Δ*uup* cells exhibited slight growth defects at both 27 °C and
446 37 °C (Fig. 3E), and the response time after a temperature upshift was substantially
447 longer (~2.7 doublings versus ~1.6 for wild type) (Fig. 3F). To examine whether this
448 difference was general to other ABC-F proteins, we examined knockouts of all other
449 ABC-F proteins (EttA, YheS, YbiT) in *E. coli*[61]. Δ*ettA,* Δ*yheS, and* Δ*ybiT* cells exhibited
450 quantitatively similar responses to wild type (Fig. S10H,I). *uup* overexpression rescues
451 the growth defect of a Δ*bipA* mutant at lower temperatures[60]; similar to Δ*uup*, growth
452 rates at 27 °C were lower than wild-type, but Δ*bipA* cells were able to accelerate to the
453 steady-state growth rate at 37 °C within 40 min, similar to wild type (Fig. S10H). Thus,
454 while Δ*uup* and Δ*bipA* mutants both have impaired ribosome assembly at lower

455 temperatures, *uup* likely serves a different function in assembly dynamics. Taken
456 together, this screen suggests that none of the nonessential genes are responsible for
457 the delayed growth-rate response to temperature upshifts.
458

459 **Response to a temperature upshift is largely conserved during antibiotic**
460 **treatment**

461 Our transposon mutant library screening was limited to nonessential genes. To
462 investigate the role of essential genes during temperature upshifts without completely
463 eliminating cell viability, we treated *E. coli* cells with a variety of antibiotics at sub-
464 minimum inhibitory concentration (MIC) levels[62] and subjected them to temperature
465 upshifts from 27 °C to 37 °C on LB. For chloramphenicol, which directly targets the
466 peptidyl transferase core of the 50S ribosomal subunit[63], growth rate decreased in a
467 dose-dependent manner at both temperatures (Fig. 3G), but the growth rate response
468 still required ~1.5 doublings based on growth under treatment at the final temperature
469 (Fig. 3G,H). Similar behavior was observed for other ribosome-targeting antibiotics: with
470 fusidic acid, which targets the translocation step in translation[64], and kasugamycin,
471 which targets translation initiation[65], growth rates were reduced and the overall
472 response time was 1.6–1.8 doublings (Fig. S11A,B). Response times were also
473 conserved under antibiotics that target DNA replication (novobiocin) and transcription
474 (rifampicin), despite large impacts on growth rate in some cases (Fig. S11C,D). Only
475 triclosan, which targets membrane synthesis, affected the response time, which
476 increased to ~2.5 doublings (Fig. 3G,H). Large spikes were present even at high
477 concentrations of triclosan (5, 10 ng/mL, Fig. S11E), while treatment with high

478 concentrations of chloramphenicol (100 μg/mL) for 15 min was sufficient to eliminate
479 any spike upon a temperature upshift (Fig. S11E), indicating that the spike requires
480 active protein synthesis and/or growth.
481
482 At high concentrations of fusidic acid (50 μg/mL), growth rate was extremely low at
483 37 °C and the normalized response time was much shorter than in untreated cells (~0.2
484 doublings; Fig. S11F,G). Given the severely limited translational capacity despite high
485 amino acid availability, these changes likely reflect a mismatch between import of
486 metabolites and the synthesis of enzymes that utilize them. Deletions of *tusA* and *tusB*,
487 genes encoding sulfur carriers important for tRNA modification[66], caused decreases in
488 growth rate due to disruption of translational elongation and the normalized response
489 time was 0.2–0.6 doublings, similar to fusidic acid treatment at high concentrations (Fig.
490 S11F,G).
491
492 Taken together, these results suggest that disruptions in core cellular processes
493 typically do not alter the normalized response time during temperature upshifts even
494 with large effects on growth rate, although in certain cases the time scale can be either
495 elongated (triclosan) or shortened (fusidic acid).
496
497 **Altered membrane fluidity has little impact on temperature-shift responses**
498 Since treatment with triclosan, which targets the fatty acid synthase FabI[67], resulted in a
499 modest increase in normalized response time (Fig. 3G,H), we hypothesized that the
500 delay in growth rate increase upon a temperature upshift might be due to the need to

501 alter membrane composition. Membrane fluidity is exquisitely regulated in *E. coli*: the
502 fraction of unsaturated fatty acids decreases with increasing temperature to maintain
503 viscosity[26,27]. To examine the impact of membrane fluidity on growth-rate dynamics, we
504 analyzed the behavior of various membrane synthesis mutants during a temperature
505 upshift from 27 °C to 37 °C on LB. FadR is a positive regulator of *fabB*, which encodes
506 the major β-ketoacyl-[acyl carrier protein] synthase responsible for elongating
507 unsaturated fatty acids[68,69], while FabR is a negative regulator of *fabB*[70]. *fadR* and *fabR*
508 deletions decreased and increased, respectively, mobility within the inner membrane
509 (Fig. 4A,B) (Methods), as expected. Previous studies suggested that, upon a
510 temperature upshift, the membrane is overly fluid and its composition is regulated to
511 restore optimal fluidity[26,27]; we found that inner membrane fluidity 5 min after the
512 temperature upshift (first measurement time point) was the same as prior to the shift
513 (Methods) (Fig. 4C), suggesting that regulation of fatty acid composition occurs over a
514 short time scale (<5 min). Moreover, Δ*fadR* and Δ*fabR* cells exhibited virtually identical
515 normalized response times as wild type (Fig. 4D,E).
516
517 Although membrane composition is regulated to maintain fluidity in wild-type cells,
518 Δ*fabR* cells grew equally fast at the single-cell level (Fig. 4D) and slightly faster and to a
519 higher yield than wild type at 37°C in liquid culture (Fig. 4F), in agreement with a
520 previous study showing that higher membrane fluidity increases growth rate and yield
521 during aerobic growth due to increased respiratory potential[27]. We reasoned that while
522 higher membrane fluidity confers a growth advantage in the Arrhenius temperature
523 range, lack of fluidity regulation may result in fitness defects at temperatures in the heat

524 shock regime due to membrane instability[71]. To test this hypothesis, we shifted wild-type
525 and Δ*fabR* cells from steady-state growth at 37 °C to 42 °C or 44 °C. Although both
526 strains were able to largely recover after a transient growth rate decrease due to the
527 upshift to 42 °C, Δ*fabR* cells experienced a larger initial decrease and took longer to
528 recover than wild type (Fig. 4G). Moreover, while wild-type cells maintained growth at
529 44 °C, Δ*fabR* cells immediately ceased growth and lost turgor pressure within 30 min
530 (Fig. 4H), presumably due to mechanical defects in the membrane permeability barrier.
531 Thus, while membrane fluidity does not determine the time scale of upshift responses,
532 its regulation is critical for cell integrity at high temperatures.
533

534 **A temperature-sensitive enzyme network (TSEN) model captures temperature-**
535 **shift response dynamics**

536 Our findings indicate that the normalized response time to temperature upshifts is
537 largely conserved (Fig. 1F,H, 2G, 3H, 4E, S5B,E, S10I, S11B,D), but can vary in certain
538 conditions (Fig. 3F,H, S5G, S11G). Our proteomic, genetic, and chemical screens
539 largely failed to uncover a key molecular regulator of the response, leaving it unclear
540 how the response behavior arises and what factors set the time scale. To interrogate
541 the mechanisms underlying these phenomena, we developed an autocatalytic network
542 model of growth. Such models have a long history in enzyme kinetics[18], and have
543 provided a useful framework for understanding emergent behaviors in gene expression
544 and bacterial growth[19,72,73].
545

To model growth, we incorporated three general classes of reactions: (1) import, (2) metabolite production, and (3) volume expansion (Fig. 5A). Each reaction obeys Michaelis-Menten kinetics, such that metabolite c_i is consumed by enzyme e_i to produce the next metabolite c_{i+1} in the network:

$$c_i + e_i \rightleftharpoons (c_i e_i)^* \longrightarrow c_{i+1} + e_i. \tag{1}$$

In a linear network (no branching), the dynamics of each intermediate metabolite are dictated by

$$\frac{dc_i}{dt} = \frac{k_{i-1} e_{i-1} c_{i-1}}{K_{i-1} + c_{i-1}} - \frac{k_i e_i c_i}{K_i + c_i} - c_i g, \tag{2}$$

where the first two terms on the right-hand side reflect enzymatic production and consumption of c_i and the last term accounts for dilution via growth at the rate g (SI). e_i is the concentration of the ith enzyme, k_i is its catalytic rate, and K_i is its Michaelis-Menten constant. Importantly, we consider the possibility that both k_i and K_i are temperature dependent with Arrhenius behavior (Fig. 5A, SI). In support of this scenario, the Michaelis-Menten constant of several enzymes has been shown to exhibit Arrhenius behavior[74-76]. After the final step of a reaction network of size *N*, an enzyme e_N consumes c_N to expand cell volume at a rate $g = \gamma_0 \frac{k_N e_N c_N}{K_N + c_N}$, where γ_0 is an efficiency factor assumed to be constant in a given environment, reflecting the conversion of c_N to a structural component of the cell envelope (SI). From physical considerations of glucose uptake and growth rate constraints (SI), we estimated that γ_0 is ~0.02 mM^{-1}. We call these equations a temperature-sensitive enzyme network (TSEN) model.

567 Since the proteome is largely maintained across temperatures (Fig. 2E, S8D), we
568 assumed that the concentration of each enzyme remains constant during any
569 temperature shift. In a simple version of our model with two intermediate metabolites
570 (minimal TSEN), we considered a single intermediate reaction between import and
571 growth and set each kinetic parameter to be identical across reactions ($k_i = 1$ min^{-1},
572 $K_i = 1$ mM at 37 °C, E_a = 15 kcal/mol). We also assumed a high (saturating)
573 concentration of the external substrate ($c_0 = 100$ mM, $K_0 = 1$ mM) and enzyme
574 concentrations of 1 mM. At a given temperature, the system reaches a steady state with
575 stable concentrations of the intermediate metabolite. The catalytic rate of 1 min^{-1} was
576 chosen for simplicity; increases in k_i that may be more representative of intracellular
577 enzymatic catalytic rates[77] have no impact on normalized growth-rate responses in the
578 model (Fig. S12A).
579
580 We simulated the model to reach a steady state at 27 °C and then shifted the
581 temperature to 37 °C. The system exhibited a non-zero response time to reach the
582 steady-state growth rate at 37 °C (Fig. 5B). To increase growth rate by 95% of the
583 difference between 27 °C and 37 °C required ~2 doublings (Fig. 5B), similar to our
584 experimental observations (Fig. 1F,H). Variations in kinetic parameters largely
585 maintained response times of 1–2 doublings (Fig. S12B). If, however, the E_a for the
586 catalytic rate of the import reaction dropped below the other catalytic rates (production,
587 growth), then the response time was instantaneous (Fig. S12B). Moreover, if the
588 activation energy for all Michaelis-Menten constants is 0, then the growth rate response
589 is also immediate (Fig. 5B), highlighting the importance of temperature sensitivity of K_i.

590 Notably, increases in the activation energy of the K_M of the production reaction
591 produced the largest increase in response times across all activation energies (Fig.
592 S12B).
593
594 To determine the key determinants of the upshift response time, we further simplified
595 the minimal TSEN to include only two reactions (import, growth) and a single
596 intermediate metabolite (c_1). This "production-less" TSEN has the benefit of being
597 analytically tractable, and predicts under a reasonable set of assumptions that the
598 steady-state concentration of c_1 is $\sqrt{\frac{K_1}{\gamma_0}}$ (SI), indicating that the temperature sensitivity of
599 c_1 and thus of growth rate is determined by the temperature sensitivity of the Michaelis-
600 Menten constant K_1. The production-less TSEN predicts that the normalized response
601 time is only non-zero when K_1 has a non-zero E_a and only weakly depends on E_a above
602 ~20 kcal/mol and K_1 above 10 mM (Fig. S12C–E, SI). Furthermore, the model predicts
603 that adaptation of the growth rate to 95% or 99% of the difference between steady-state
604 growth rates at the two temperatures occurs within 0.8 or 1.9 doublings, respectively
605 (Fig. S12F, SI), consistent with our experimental data and suggesting that the precise
606 definition of the response time scale is not critical for producing physiological
607 timescales.
608
609 For a reaction network with *N* intermediates, the analytical solution of steady-state
610 growth rate (SI) is

611 $$g = \frac{\frac{k_0 e_0 c_0}{K_0 + c_0}}{\frac{1}{\gamma_0} + \sum_{i=1}^{N} c_i}, \quad (3)$$

612 which is set by the import rate $\frac{k_0 e_0 c_0}{K_0 + c_0}$, growth efficiency factor γ_0, and the total

613 intracellular metabolite concentration $\sum_{i=1}^{N} c_i$. Since import changes instantaneously with

614 temperature, the response time scale is associated with rearrangement of the

615 metabolome. Eq. 3 also reflects that growth comes at the cost of storing metabolic

616 intermediates c_i, and holds regardless of branching within the network (SI). This model

617 recovers the well-known Monod Equation as long as import follows Michaelis-Menten

618 kinetics[78] (SI), which has been shown for a variety of sugar transporters in *E.* coli[77,79,80].

619 Eq. 3 also predicts a growth rate in glucose consistent with estimates derived from

620 glucose uptake rates (SI). Additionally, as metabolite concentrations and import rate

621 both increase with temperature, the growth rate (g) can exhibit some slight non-

622 Arrhenius temperature dependence (Fig. S12G).

623

624 In *E. coli*, the majority of major metabolites are present at concentrations that saturate

625 their respective enzymes[81]. However, many central-carbon reactions operate near their

626 K_M[81], suggesting that bottlenecks are highly likely. Moreover, enzymes that catalyze

627 product formation tend to have higher activation energy than transporters[82]. Within a

628 simple network involving import, production, and growth, introducing a bottleneck into

629 the production reaction characterized by a large and temperature-sensitive K_M

630 ($K_M(T = 37\,°\mathrm{C}) = 20\ \mathrm{mM}$, E_a=22 kcal/mol) produced strikingly physiological behavior:

631 simulations predicted an initial spike similar to our experimental observations and a

632 response time of ~2 doublings (Fig. 5B). Moreover, when the bottleneck was within a

633 pathway involving multiple production reactions, the spike broadened, and the
634 acceleration dynamics were quantitatively similar to our experimental measurements
635 (Fig. 5C). This TSEN model readily predicts asymmetric behavior between upshifts and
636 downshifts (Fig. 5D); such asymmetry is expected from temperature-dependent
637 Michaelis-Menten kinetics[12]. Additionally, after the initial large decrease in growth rate
638 upon a downshift, the multiple-reaction model predicts a slow deceleration toward the
639 slower steady-state growth rate (Fig. 5D, dark blue), similar to our experimental
640 observations (Fig. 1C, S2). Thus, an initial spike, a physiological response time, and
641 asymmetric behavior emerge from only a few simple assumptions about the network.
642

643 **Spike and response time are dictated by metabolome rearrangement**

644 In the bottlenecked TSEN model, metabolites after the bottleneck undergo a transient
645 decrease in concentration after a temperature upshift (Fig. 5E) that agrees with the time
646 scale of the spike response (Fig. 5D), suggesting that spikes are caused by rapid
647 consumption of post-bottleneck metabolites. Meanwhile, metabolites before the
648 bottleneck gradually build up, as do the post-bottleneck metabolites after the spike, until
649 metabolome rearrangement has stabilized (Fig. 5E). As a result, final growth rate (which
650 scales with temperature) dictates the thermally limited response time necessary to
651 rearrange the metabolome. Simulations of our model captured the near invariance of
652 the normalized response time across initial and final temperatures (Fig. 5F) as
653 represented by linear scaling of absolute response time with doubling time at the higher
654 temperature (Fig. 5G). This scaling was consistent with our experimental measurements
655 (Fig. 2E), which exhibited a slope of 1.4±0.3 (Fig. 5H), consistent with the range of

normalized response times measured across temperatures and growth media (Fig. 1F,H).

Growth rate follows the Monod Equation in a temperature-dependent manner

Our model indicates that the temperature sensitivity of K_M is a critical determinant of the response to temperature upshifts, motivating us to broadly explore K_M over temperatures and nutrients. Early work by Monod and others demonstrated that *E. coli* growth rate depends on glucose concentration in a manner remarkably similar to Michaelis-Menten enzyme kinetics with a half-saturation constant K_M~22 μM[78]. This relationship is referred to as the Monod Equation

$$g = \frac{g_{\max} c}{K_M + c}, \tag{4}$$

where c is the concentration of the substrate (e.g., glucose) and $g_{\max}$ is the growth rate when $c \gg K_M$. Theoretically, a temperature-dependent K_M should cause the overall activation energy to decrease at lower substrate concentration, making growth less temperature sensitive[12]. Previous studies indicated that growth of *E. coli* on simple sugars generally obeys the Monod Equation[83], with a range of reported K_M values[84]; *E. coli* growth on acetate has a particularly large K_M~8 mM[85]. The K_M of *E. coli* growth on glucose is small[86] and has been hypothesized to be invariant across temperatures[84]. The K_M for the growth of nitrifying bacteria on nitrogen is temperature dependent[87], as is the K_M for the growth of *Methanosarcina barkeri* on acetate[88] and of *Klebsiella aerogenes* on glucose[89]. Thus, growth rates generally obey Michaelis-Menten kinetics, with K_M values that can vary over many orders of magnitude and with unclear temperature dependence.

679

680 To examine the temperature dependence of K_M across a diverse range of metabolizable
681 substrates, we grew *E. coli* MG1655 in MOPS minimal medium supplemented with
682 simple sugars (glucose, fructose, maltose), succinate, acetate, or casamino acids at
683 various concentrations and temperatures (25 °C, 30 °C, 37 °C) and quantified maximum
684 growth rate in liquid culture (Methods). We also measured growth rate across
685 concentrations of LB, whose average stock amino acid molarity we estimated to be 182
686 mM (Methods). In glucose, we estimated that K_M at 37 °C was 36±13 μM, in reasonable
687 agreement with early work by Monod[78] (Fig. S13A–C). At lower temperatures (25 °C,
688 30 °C), measuring growth rates at concentrations <150 μM was challenging (Fig. S13B),
689 but our estimated values (Fig. S13C) were in reasonable agreement with the reported
690 K_M for the glucose-specific transporter PtsG in *E. coli* (60 μM)[79]. In other sugars, we
691 measured a wide range of K_M values (Fig. S13A,C) consistent with previous studies[80].
692 For growth on casamino acids or LB, K_M was relatively large and clearly increased with
693 temperature (Fig. S13A,C). These data indicate that the K_M for non-sugar substrates
694 can be at least an order of magnitude higher than for simple sugars and temperature
695 dependent. However, on some substrates K_M remained constant or even decreased
696 with increasing temperature (succinate, maltose; Fig. S13C).

697

698 These measurements also enabled estimation of the activation energy for growth in
699 each condition (Fig. S13D–G). In glucose, E_a was relatively constant (22±6 kcal/mol)
700 between 0.17 mM and 11 mM (Fig. S13D,F), which are concentrations >3-fold above
701 K_M (40-60 μM); this activation energy is substantially higher than in LB. For growth on

acetate, amino acids, and LB, we were able to measure E_a accurately at concentrations below K_M. On acetate, E_a decreased from 27±6 kcal/mol during growth at saturation to 19±4 kcal/mol at half the K_M (3.8 mM) (Fig. S13F). On amino acids or LB, E_a decreased from 16±4 kcal/mol or 15±2 kcal/mol, respectively, at saturation to 4±2 kcal/mol at 0.9 mM or 6.5±5 kcal/mol at 0.6 mM, respectively (Fig. S13E,G). Thus, for substrates with large K_M (>1 mM), the activation energy for growth decreases with concentration, as expected for simple enzyme behavior[12].

TSEN model predicts spike dependence on nutrient type and the response to a downshift pulse

Despite the higher temperature sensitivity (E_a) of steady-state growth rate in glucose compared with CAA or LB, the response time for an upshift was highly similar across these nutrients (Fig. 1H), as predicted by our TSEN model, wherein increases in the activation energy of the import reaction have little effect on response times (Fig. S12B). However, the spike was much smaller or nonexistent in glucose as well as glycerol (Fig. 1H), another condition in which E_a was much larger than in LB (Fig. S13F,G). Motivated by this decoupling of response time and spike height, we probed the behavior of our model when changing the activation energy of the catalytic rate of the import reaction to mimic the differences between LB and glucose. Our model predicts that spike height should decrease sharply when the activation energy of import is >15 kcal/mol (Fig. 6A). An increase from 15 kcal/mol to 30 kcal/mol (with all other parameters held constant) lowered the growth rate at 27 °C by approximately 40% and dramatically lowered the spike height (Fig. 6B). However, the response time increased by only ~0.1 doubling

725 (Fig. 6B), as the rest of the TSEN model parameters remained unaltered. Thus, the
726 model predicts that activation energy differences between nutrient types (Fig. S13F,G)
727 are sufficient to explain our experimental data for the response dynamics in simple
728 sugars and lacking amino acids (Fig. 2G,H).
729
730 While growth rate rapidly decreases after a downshift in our model (Fig. 5D), the
731 concentration of metabolites requires dilution to equilibrate, which takes place on the
732 time scale of growth. Thus, during a transient downshift pulse, the cell gradually
733 transitions from the high temperature to the low temperature metabolic state. Indeed,
734 simulations of the bottle-necked TSEN model (Fig. 5C) during a downshift pulse from
735 37 °C to 27 °C back to 37 °C, with variable duration at 27 °C, resulted in faster upshift
736 responses than from the steady state at 27 °C (Fig. 6C). More than a doubling at 27 °C
737 was required for recovery of the upshift response time (Fig. 6D) and the spike height
738 remained higher than for an upshift from steady state for pulses of multiple doublings
739 (Fig. 6E), again collectively consistent with our experimental data (Fig. 1I, S7).
740
741 These findings highlight the ability of our model to reproduce nearly all observed
742 temperature-shift responses with reasonable quantitative agreement, and underscore
743 the importance of the temperature sensitivity of import and metabolome rearrangement
744 in upshift responses.
745
746 **TSEN model successfully predicts temperature upshift response at low substrate**
747 **concentration**

748 Although we have thus far focused on experimental conditions in which the external
749 substrate concentration is saturating, nutrient concentrations are low in many
750 environments[90,91]. Since a key feature of the ability of our model to successfully predict
751 upshift responses is the temperature sensitivity of Michaelis-Menten constants, we were
752 motivated to examine the low-nutrient regime. Microbes typically respond to low-nutrient
753 conditions by upregulating stress response pathways and altering their proportions of
754 import and biosynthesis enzymes[91,92], but such regulatory mechanisms occur on much
755 longer time scales than a rapid temperature upshift, hence we kept all parameters in the
756 model constant besides substrate concentration. We simulated our model with external
757 concentrations below the K_M for import and considered a temperature upshift from
758 27 °C to 37 °C. At $c_0 < K_0$, the relative spike height increased substantially, up to 100%
759 of the steady-state growth rate difference between the two temperatures, and the
760 normalized response time decreased with decreasing concentration (Fig. 6F–J). This
761 decrease in response time occurred because the increase in import rate after a
762 temperature upshift is smaller when $c_0 \leq K_0$ compared with $c_0 \geq K_0$[12], despite an
763 identical increase in catalytic rates that consume the imported metabolite. The activation
764 energy for growth was also predicted to decrease with decreasing nutrient concentration
765 (Fig. 6H), in agreement with our experimental measurements of growth on amino acids
766 (Fig. S13G).
767
768 To test these predictions, we shifted MG1655 cells from 27 °C to 37 °C during growth
769 on MOPS minimal medium supplemented with a low concentration of casamino acids
770 (CAA) (Methods). With 4.6 mM CAA, a concentration near the K_M, growth rate

771 increased from the steady state value at 27 °C (~0.5 h^{-1}) to that at 37 °C (~0.8 h^{-1}) after
772 only 25 min, corresponding to 0.25 doubling times at 37 °C (Fig. 6K,L). Moreover, the
773 spike peaked at a growth rate close to that of the 37 °C steady state (Fig. 6K). These
774 dynamics were in reasonable agreement with the predictions of our model (Fig. 6I,J),
775 indicating that the response to temperature shift is dictated by the temperature
776 sensitivity of K_M and its relationship with nutrient concentration.
777

778 **Diverse bacteria exhibit a characteristic response to temperature shifts**

779 We sought to determine if other strains and species would exhibit similar responses to
780 temperature upshifts as *E. coli* MG1655 and BW25113. We first examined several *E.*
781 *coli* strains during a temperature upshift from 25 °C to 37 °C on LB. *E. coli* CS109, a K-
782 12 strain that has impaired lipid synthesis and is defective in growth at temperatures
783 above 37 °C (Fig. S1D,E)[93], exhibited the characteristic spike and linear acceleration
784 from 0.8 h^{-1} to 1.8 h^{-1} within ~33 min (Fig. 7A), corresponding to a normalized response
785 time of ~1.4 doublings (Fig. 7B). An *E. coli* isolate from a human fecal sample exhibited
786 faster steady-state growth rates than MG1655 or BW25113[94], and an upshift caused a
787 spike and overall increase from 1 h^{-1} to 2.3 h^{-1} within 30 min (Fig. 7A), corresponding to
788 a normalized response time of ~1.6 doublings (Fig. 7B). *E. coli* isolates from a turtle
789 (cold-blooded host, strain Ram551) and a seagull (high host body temperature,
790 Ram1897) displayed similar responses, with a spike and linear acceleration that in total
791 required 1.5 and 1.7 doublings, respectively (Fig. 7A,B). Additionally, each of these
792 strains responded to the downshift from 37 °C to 25 °C on the time scale of the

temperature dynamics (Fig. S14). Thus, diverse strains of *E. coli* exhibited a common characteristic response.

In the gut commensal *Escherichia fergusonii* B253, the temperature shift from 25 °C to 37 °C resulted in a growth rate increase from 1 h^{-1} to 2.3 h^{-1} with a spike and subsequent linear acceleration over ~30 min (Fig. 7A), corresponding to a normalized response time of 1.5 doublings (Fig. 7B). In the Gram-positive *Bacillus subtilis* 168, an upshift from 27 °C to 37 °C produced a large spike from ~0.7 h^{-1} to ~1.3 h^{-1} that extended several minutes longer than in *Escherichia* strains, and then growth rate linearly accelerated to ~2.0 h^{-1} (Fig. 7A). The entire response lasted ~45 min, producing a normalized response time of ~2 doublings (Fig. 7B). Additionally, both species responded rapidly to downshifts (Fig. S14), similar to *E. coli.* These results suggest that bacteria generally respond to temperature shifts with a characteristic spike and linear acceleration requiring 1.4–2 doublings at the final temperature, and that metabolic differences between phylogenetically diverged species may result in subtle distinctions in the upshift response.

Temperature shifts in fission yeast produce a distinct response captured by the TSEN model

We sought to determine if single-celled eukaryotes would respond to temperature shifts in a similar manner to bacteria. The rod-shaped fission yeast *Schizosaccharomyces pombe* grows optimally at 32 °C and possesses an Arrhenius range between 22 °C and 32 °C, with E_a~8 kcal/mol in rich media[95]. During an upshift on the rich medium YE5S

816 from 22 °C to 32 °C, cells exhibited a large growth-rate spike from 0.17 h^{-1} to 0.44 h^{-1},
817 overshooting the steady-state growth rate at 32 °C (Fig. 7C). This spike was
818 immediately followed by a deceleration to 0.02 h^{-1}, followed by rapid acceleration to the
819 steady-state growth rate at 32 °C (~0.4 h^{-1}) (Fig. 7C). The entire response dynamics
820 lasted ~100 min, corresponding to a normalized response time of ~1.1 doublings (Fig.
821 7D). Thus, despite decelerating to near growth halting, *S. pombe* cells were able to
822 reach the steady-state growth rate at the higher temperature more quickly than any
823 bacteria tested at saturating nutrient concentration.
824
825 We wondered whether these differences in behavior were consistent with our TSEN
826 model. By varying key model parameters and the number of bottleneck reactions, we
827 identified networks with dynamics upon temperature upshift that closely matched those
828 of *S. pombe*, with faster normalized response time when the E_a of the bottleneck K_M
829 was increased to >30 kcal/mol and the bottleneck enzymatic rate was greater than
830 those of import and growth. Moreover, a TSEN composed of 5 bottlenecked
831 intermediate reactions resulted in a more pronounced spike and deceleration (Fig. 7D),
832 similar to our experimental measurements (Fig. 7C,D). The large spike and deceleration
833 were due to rapid consumption of the network's final metabolite (c_6), which could only
834 be replenished by upstream bottlenecked metabolites (Fig. 7E). The overall faster
835 response time was captured by the model and was due to the decrease in steady-state
836 concentration of c_6 at higher temperature caused by the large E_a of K_M (Fig. 7E),
837 leading c_6 (which is limiting for growth) to stabilize more quickly.
838

With the same set of parameters, this TSEN model also predicted an under-shooting to below the new steady-state growth rate upon a temperature decrease from 32 °C to 22 °C (Fig. 7F), a nonintuitive behavior we confirmed experimentally (Fig. 7F). These findings suggest that the qualitatively distinct characteristics of the *S. pombe* temperature shift responses can be captured in a TSEN model by increasing the magnitude of K_M parameters and the number of bottleneck reactions, and more generally that the growth network can be tuned to alter the balance between certain tradeoffs, to accelerate responses at the cost of temporary growth stalling.

847 **Discussion**

848 Here, we used high-precision temperature control and single-cell analyses to show that
849 bacteria exhibit characteristic growth-rate responses to temperature shifts within the
850 Arrhenius range (Fig. 1C, 7A). Temperature upshifts produced a gradual, multi-step
851 acceleration (Fig. 1C), with a normalized response time of ~1.5 doublings at the final
852 growth rate that was invariant across temperatures (Fig. 1F) and substrates (Fig. 1H)
853 and independent of whether there was an initial spike in acceleration, as observed
854 during growth on amino acids but not on simple sugars (Fig. 1H). Moreover, the spike
855 and subsequent linear acceleration as cells transiently grown at 47 °C were returned to
856 37 °C (Fig. S6B) suggests similar underlying adaptation as for upshifts in the Arrhenius
857 range. Conversely, temperature downshifts produced a rapid deceleration (Fig. 1B, S3,
858 S14). Downshift pulse experiments revealed a memory whereby cells exposed to low
859 temperatures for short durations can respond much more quickly to temperature
860 upshifts (Fig. 1I, S7), an effect that persists for more than a doubling at the lower
861 temperature. Thus, it is likely that some subset of intracellular components changes with
862 temperature and that growth is required to dilute, given the duration required to erase
863 the memory effect.

864

865 The maintenance of the proteome across temperatures (Fig. 2) and the conservation of
866 response dynamics during upshifts across mutants (Fig. 2G, 5E, S10I) and antibiotic
867 treatments (Fig. 3H, S11B,D) collectively argue against the existence of a single
868 regulator of growth rate across Arrhenius temperatures. Instead, the ability of our TSEN
869 model to recapitulate nearly all observed behaviors (Fig. 5,6, S12) indicates that

870 temperature sensitivity of growth is a collective property of the metabolic network. A key
871 feature is the temperature dependence of K_M, which provides a straightforward
872 mechanism for the asymmetry between upshift and downshift responses (Fig. 7F): if the
873 substrate concentration of a reaction is near the K_M at 27 °C (Fig. 7F, blue circle), an
874 upshift to 37 °C will be accompanied by a small instantaneous growth rate increase
875 since K_M is higher at 37 °C versus 27 °C; vice versa, a downshift from the K_M at 37 °C
876 (Fig. 7F, red circle) will result in a larger instantaneous change in growth rate (Fig. 7F).
877 Each of these instantaneous changes is then followed by an increase (upshift) or
878 decrease (downshift) in the substrate concentration, and thus the growth rate (Fig. 7F),
879 as predicted by the TSEN model (Fig. 5E, SI).
880
881 To produce the observed initial spike in growth rate, a bottleneck reaction with a large
882 and highly temperature-sensitive K_M was required (Fig. 5C). Previous measurements of
883 intracellular metabolite dynamics in *E. coli* grown on glucose showed that reactions in
884 central carbon metabolism are largely unsaturated and many reactions can exhibit large
885 K_M values (>1 mM)[81] (Fig. 7G), indicating that the existence of such bottlenecks is
886 highly likely. There are a large number of potential bottleneck enzymes (Fig. 7G); those
887 with the largest substrate concentrations are involved in aspartate consumption for
888 amino acid (*aspC*) and pyrimidine (*pyrB*) biosynthesis, while those with the largest K_M
889 are involved in threonine (*ilvA*) and serine *(sdaA*, *ydfG)* degradation. As several of these
890 reactions are essential, elucidating which reactions are true bottlenecks will likely
891 require a combination of CRISPRi manipulation of gene expression, direct

892 measurements of intracellular metabolite concentrations[81], and biochemical
893 characterization across temperatures.
894
895 Although our TSEN model involves 5 parameters per enzymatic reaction, the activation
896 energies are reasonably constrained by observed measurements (8–30 kcal/mol)[13,96],
897 and the predicted dynamics are largely insensitive to many of the chosen parameters
898 (Fig. S12). Furthermore, specific details of the network architecture (e.g., branching)
899 have no effect on the qualitative predictions of the TSEN model (SI). Most importantly,
900 the analytically tractable production-less TSEN model predicts that response times are
901 constrained to 1–3 doublings, regardless of kinetic parameter values (SI).
902
903 At steady state, the TSEN model predicts that growth depends only on substrate import
904 kinetics and the total intracellular metabolite pool (Eq. 3), recovering the empirical
905 Monod Equation (Eq. 4) and providing a simple framework that connects concentration-
906 dependent growth directly to measured transporter kinetics[77], thus establishing a simple
907 mechanism for how Arrhenius-like growth arises across organisms[10]. Our finding that
908 import K_M values for simple sugars are generally small (<200 μM) and approximately
909 temperature insensitive (Fig. S13C,F) is in agreement with previous measurements in
910 glucose[86] and suggests that the activation energy of each rate constant is similar for
911 simple sugars[12]. However, growth on other carbon sources or amino acids produced
912 large (1-10 mM) and temperature-sensitive K_M values (Fig. S13C). Why K_M values for
913 sugars in *E. coli* are temperature insensitive is unclear, although the K_M values for the
914 vast majority of enzymatic reactions are thought to be temperature sensitive[13]. The

915 temperature upshift response is predicted to be largely insensitive to the K_M of import at
916 substrate saturation (Fig. 6F), suggesting that temperature-shift responses are
917 independent of the details of import kinetics.
918
919 A temperature-sensitive K_M predicts that the E_a of growth rate will decrease with
920 substrate concentration[12] (Fig. 6H), consistent with our measurements of growth on
921 amino acids (Fig. 6K,L). Such a decrease in temperature sensitivity at low substrate
922 concentration is predicted by the TSEN to decrease the response time and increase the
923 relative spike height (Fig. 6F,G,I,J), consistent with our experimental observations that
924 decreases in amino acid concentrations resulted in faster responses to temperature
925 upshifts and larger relative spikes (Fig. 6K,L). Thus, microorganisms confronting
926 nutrient-poor environments may exhibit less temperature sensitivity of growth,
927 somewhat paradoxically owing to the temperature sensitivity of K_M values.
928
929 Additionally, the TSEN model was able to explain qualitatively distinct temperature shift
930 responses in the fission yeast *S. pombe*, which responded to an upshift with
931 overshooting and deceleration (Fig. 7C), but which ultimately reached its steady-state
932 growth rate faster than bacteria (Fig. 7D). The TSEN model predicted that large,
933 coupled bottleneck reactions account for this behavior (Fig. 7D,E), and such a model
934 predicted the undershoot response to a temperature downshift (Fig. 7F). In this
935 scenario, faster temperature-shift responses come at the cost of increasing the
936 activation energy of growth (Fig. 7C,F), further suggesting tradeoffs between fast

937 steady-state growth across temperatures and the ability to respond quickly to shifts
938 between temperatures.
939
940 Taken together, these findings suggest that metabolite flux rather than proteome
941 rearrangement underlies growth rate adaptation across Arrhenius temperatures. As a
942 result, cells adapt to temperature fluctuations without additional protein synthesis,
943 resulting in transient memory of previously experienced temperatures (Fig. 2I, S7, 6C–
944 E). Proteins comprise ~55% of the cell's biomass[97] but constitute a relatively small total
945 concentration ~7 mM[81] compared with metabolites, which make up ~300 mM despite
946 being only ~3% of biomass[81,97]. Thus, increasing protein concentrations is metabolically
947 expensive, and simulations of our TSEN model explicitly including protein synthesis
948 confirmed that enzyme concentrations remain virtually constant throughout temperature
949 shifts (Fig. S15). The conservation of growth rate responses across organisms (Fig. 7A–
950 D), and the ability of the TSEN model to capture diverse responses to temperature
951 shifts (Fig. 5–7) suggests an evolutionary pressure to adopt this strategy. The ability of
952 *E. coli* cells to withstand fluctuations across a large range of temperatures, even short
953 pulses at heat- and cold-shock temperatures (Fig. S6B,C,E), indicates a robustness that
954 may be particularly important in the context of host colonization and infection-induced
955 fevers, and our findings indicate that investigations of temperature adaptation can
956 provide key insight into the metabolic factors limiting growth.
957

958 **Acknowledgements**

959 We thank members of the Huang lab for helpful discussions. The *E. coli* BW25113
960 transposon mutant library was provided by the Deutschbauer lab, with help from
961 Valentine Trotter. This work was funded by a Stanford Interdisciplinary Graduate
962 Fellowship (to B.D.K.), NIH RM1 GM135102 (to K.C.H.) and NSF Awards EF-2125383
963 and IOS-2032985 (to K.C.H.). K.C.H. is a Chan Zuckerberg Biohub Investigator.

964 **Methods**

965

966 **Culturing conditions and bacterial strains**

967 *E. coli* wild-type and isolate strains were grown directly from 25% glycerol stocks stored
968 at -80 °C in target media without selection. In typical temperature upshift experiments,
969 cells were grown initially at 37 °C from frozen stocks overnight until saturation, then
970 diluted 1:200 into fresh media at 37 °C until log phase (1.5–2 h in LB, ~4 h in MOPS +
971 glucose). Cells were then diluted 1:10 into fresh media and grown for at least 3
972 doublings at the lower, target temperature before performing a temperature upshift.

973

974 Most mutants (e.g., Keio collection knockouts) were grown from frozen stocks in target
975 media with antibiotic selection. The ppGpp null strain (*spoT::cat, relA::kan*) was grown
976 on LB plates with 10 µg/mL chloramphenicol and 25 µg/mL kanamycin overnight at
977 37 °C, and individual colonies were selected for further liquid culturing under selection
978 to avoid suppressor mutations.

979

980 To evaluate growth kinetics on various media, *E. coli* MG1655 was first grown shaking
981 overnight at 37 °C in MOPS minimal medium (Teknova, Hollister, CA) adjusted to pH
982 7.2 supplemented with 0.2% (w/v) D-glucose. To measure growth at lower temperatures
983 (25 °C, 30 °C), cells were then diluted 1:200 in fresh MOPS+glucose and grown shaking
984 until saturation for an initial passage at the target temperature. One milliliter of cells
985 were washed in MOPS buffer (pH 7.2) at room temperature and 1 µL was added to 200

986 μL of target medium in 96-well plates for generating growth curves at the target
987 temperature in a plate reader.
988
989 All strains used in this study are listed in Table S1.
990
991 **Liquid growth curves and analysis**
992 Growth curves were measured using a protocol developed for accurately determining
993 growth rates at low optical density[98]. Briefly, 200 μL of medium (without bacteria) were
994 placed into each well of a transparent 96-well plate (Greiner Bio-One, Monroe, NC) and
995 sealed with a transparent film (Excel Scientific, Victorville, CA) with holes for gas
996 exchange cut above each well using a laser cutter (Epilog, Golden, CO). Optical density
997 (OD) was measured with a BioTek Epoch 2 microplate spectrophotometer (Agilent,
998 Santa Clara, CA) for at least 15 min to obtain blank values for each well at the target
999 temperature. The seal was then removed, bacterial samples were added into each well,
1000 and the plate was sealed with a fresh laser-cut transparent film. Linear and orbital
1001 shaking were conducted between OD readings, which were taken every ~7 min. The
1002 OD was corrected for non-linearity (linear range = 0–0.6) via a serial dilution of
1003 concentrated cells and performing a polynomial fit to obtain general fit parameters [98].
1004 For each well, the well-specific blank OD value determined prior to addition of cells was
1005 subtracted from the OD at each time point, which was then used to computed growth
1006 rate as a moving linear regression of the logarithm of the blanked OD.
1007
1008 ***E. coli* natural isolates**

1009 *E. coli* strains from non-human hosts were previously isolated[32,33,99] from fecal samples
1010 collected from a variety of sources, including park and pet store animals and domestic
1011 pets, which were grown on Colilert-18 medium (IDEXX, Portland, ME) for selection of
1012 presumptive *E. coli* colonies[33]. Isolate identities were confirmed by beta-glucuronidase
1013 activity and subsequent sequencing of the corresponding gene, *uidA*[33]. The strains were
1014 grown overnight in a rich medium (LB) at 37 °C, diluted 1:200 in fresh LB, and grown for
1015 24 h across temperatures from 27 °C–47 °C to measure activation energies.
1016

1017 **Temperature-controlled single-cell imaging**

1018 The temperature control platform, the Single-Cell Temperature Controller (SiCTeC),
1019 was designed and described previously[39]. Briefly, a ring-shaped Peltier module (TE
1020 Technology, Traverse City, MI) was adhered to a glass slide, and the sample
1021 temperature was monitored on the coverslip and controlled using a micro-Arduino with a
1022 proportional-integral-derivative (PID) algorithm. Sample temperature was monitored and
1023 visualized in real time using the open-source software Processing[100]. Agarose
1024 hydrogels were prepared by boiling 3% ultrapure agarose (Sigma Aldrich, St. Louis,
1025 MO) in the target medium, and 200 μL of the mixture were pipetted onto a 9-mm
1026 diameter silicone gasket (Grace Bio-Labs, Bend, OR) onto the temperature-controlled
1027 glass slide. An additional slide was placed on the gasket to compress the hydrogel,
1028 which then cooled and solidified at the initial temperature of the experiment. After
1029 removing the additional compressing slide, 1 μL of cells was pipetted onto the solidified
1030 hydrogel and dried briefly (<1 min) at the initial temperature of the experiment.
1031

1032 Imaging was performed on a Ti-Eclipse microscope in phase-contrast mode using a
1033 40X Ph2 air objective (NA: 0.95) (Nikon Instruments, Tokyo, Japan) with a 1.5X tube
1034 lens. The air objective was used to avoid heatsink issues with oil-immersion objectives.
1035 Images were captured every 30 s on a Zyla 4.2 sCMOS (Andor Technology, Belfast,
1036 UK), Neo 5.5 sCMOS (Andor Technology, Belfast, UK) or PCO Panda 4.2 (Excelitas,
1037 Pleasanton, CA) scientific camera. The microscope system was integrated using
1038 μManager 1.41[101].
1039

1040 **Image analysis**

1041 To extract cell morphology information throughout the experiment, subpixel-resolution
1042 cellular contours were obtained through a combination of deep learning-based and
1043 traditional image segmentation software[39,102]. Briefly, we first aligned the images using
1044 the Template-Matching plugin in FIJI[103,104], then each image was processed with a fully
1045 convolutional neural network model, *DeepCell*[102]. Separate neural networks were
1046 trained for *E. coli* rich medium, *E. coli* minimal medium, and *S. pombe* rich medium,
1047 with >200 cells manually annotated in each condition[39,40,102]. Outputs from DeepCell
1048 classification were used to extract cellular contours using *Morphometrics* v. 1.1 in
1049 MATLAB (MathWorks, Natick, MA)[105]. Custom MATLAB scripts were used to track
1050 individual cells and measure cellular geometry[40].
1051

1052 **Rapid temperature downshifts**

1053 To increase the rate of temperature change during downshifts from previous
1054 experiments performed using ambient temperature as the cooling sink, which required

1055 ~5 min from 37°C to 27 °C[39], we used dry ice (solid CO_2) to rapidly cool samples.
1056 During a downshift, the SiCTeC device was powered off and a 250-mL beaker with dry
1057 ice was used to pour sublimating dry ice directly onto the sample on the glass slide. For
1058 downshifts to temperatures above ambient, when the temperature was ~1 °C above the
1059 target downshift temperature, the SiCTeC device was powered back on and the PID
1060 algorithm restarted control of the sample temperature. The sample temperature was
1061 closely monitored and adjusted accordingly for undershooting. This method enabled
1062 stabiliziation at the lower temperature within <1 min. For downshifts to temperatures
1063 below ambient, dry ice was continuously poured onto the sample at intervals necessary
1064 to maintain the target temperature. Temperature upshifts back to 37 °C were performed
1065 by turning back on the SiCTeC device.
1066

1067 **Anaerobic growth**

1068 To perform temperature shifts in anerobic conditions, *E. coli* MG1655 was inoculated
1069 from a frozen stock into LB and grown overnight in an anaerobic chamber (Coy
1070 Laboratory Products, Grass Lake, MI), then diluted 1:200 and grown until saturation in
1071 pre-reduced LB (i.e., kept in chamber for >48 h before culturing). Cells were diluted
1072 1:200 in pre-reduced LB and grown at 37 °C until log phase (~2 h), then diluted 1:10
1073 and grown at 27 °C for 3 h. From log phase at 27 °C, 1 μL was pipetted on a SiCTeC
1074 glass slide for temperature shifts (all components pre-reduced) and imaged inside the
1075 chamber using a Ti-Eclipse inverted microscope (Nikon Instruments, Tokyo, Japan) with
1076 a Neo 5.5 sCMOS (Andor Technology, Belfast, UK). The SiCTeC platform was
1077 controlled by a laptop inside the chamber.

1078

1079 **Quantification of response time**

1080 To measure the response time of an upshift trajectory, the steady-state growth rate (g^{ss})
1081 at the final temperature was determined by measuring the average of the growth rate
1082 across the timepoints after which growth rate had stabilized (determined by visual
1083 inspection). Its error (δg^{ss}) is defined as the standard error of the mean. This steady-
1084 state growth rate was subtracted from the entire trajectory ($g(t) - g^{ss}$), and the
1085 response time was determined as the time (t) at which $g(t)$ was indistinguishable from
1086 g^{ss} within error (δg^{ss}), which was generally ~5% of g^{ss}.

1087

1088 **Antibiotic treatment during single-cell temperature shifts**

1089 Five-hundred microliter aliquots of growth medium+3% ultrapure agarose were melted
1090 at 95 °C, then mixed with 0.5 μL of 1000X target concentration antibiotic stock solution
1091 and 150 μL was immediately used to make a hydrogel for the sample as described
1092 above. The short time exposed to higher temperatures (~30 s) likely only moderately
1093 impacted the minimum inhibitory concentration, as antibiotic efficacies against *E. coli*
1094 are unaffected by long-term (30 min) treatment at 56 °C, with many drugs unaffected by
1095 autoclaving (121 °C)[106].

1096

1097 **Liquid culture samples for proteome extraction**

1098 *E. coli* MG1655 was grown at 37 °C overnight in MOPS buffer (Teknova, Hollister, CA)
1099 adjusted to pH 7.2 supplemented with 0.2% (w/v) of carbon source (glucose or glycerol)
1100 (Sigma-Aldrich, St. Louis, MO) or LB (Thermo Fisher Scientific, Waltham, MA), then

1101 diluted in duplicate and grown for at least 4 doublings at the target temperature (25 °C,
1102 30 °C, or 37 °C). Growth at additional temperatures (16 °C, 43 °C) were assayed for LB.
1103 Cultures were grown to log phase (OD_{600}~0.2) in 50-mL Falcon tubes and 15 mL were
1104 harvested and washed with 1 mL PBS via centrifugation at 4 °C. Supernatant was
1105 removed and the pellet was snap-frozen with liquid nitrogen.
1106

1107 **Proteome extraction**

1108 Extraction was performed as previously described[107]. Briefly, samples were thawed and
1109 lysed using a bead-beating procedure, then supernatant was reduced and alkylated with
1110 DTT and iodoacetamide, respectively. Peptides were then washed, digested, and eluted
1111 using S-trap tubes (Protifi) and desalted with C18 solid-phase extraction (Sep-Pak
1112 Waters). Finally, peptides were dried by vacuum centrifugation and quantified for
1113 normalization (Nanodrop ND-1000).
1114

1115 **Proteomic analysis via LC-MS/MS and database searching**

1116 Peptide quantification was performed as previously described[107]. Briefly, dried peptides
1117 were diluted in 0.2% formic acid to a final concentration of 0.5 μg/mL, then separated by
1118 reversed-phase chromatography (Dionex Ultimate 3000 HPLC, Thermo Fisher
1119 Scientific, Waltham, MA) and directed to a LTQ Orbitrap Elite mass spectrometer
1120 (Thermo Fisher Scientific, Waltham, MA). The top 20 ions were selected for
1121 fragmentation using collision-induced dissociation (DIC), and fragments were analyzed
1122 in the ion trap with rapid scan rate.
1123

1124 Mass spectra were searched against the UniProt canonical *E. coli* FASTA database
1125 using the SEQUEST algorithm of Proteome Discoverer 2.2.0.388. Peptides were filtered
1126 using Percolator with the protein false discovery rate set to 1%. Protein abundance was
1127 based on precursor ion peak areas.
1128

1129 **Proteome data analysis and annotation using Clusters of Orthologous Groups**
1130 **(COG)**

1131 Protein functional annotation was performed using the Clusters of Orthologous Groups
1132 of proteins (COG) database[58]. UniProt accession codes were mapped to the COG
1133 database downloaded from https://ftp.ncbi.nih.gov/pub/COG/COG2014/data/. The
1134 corresponding gene of each protein was annotated using the gene association table
1135 from EcoCyc (https://ecoliwiki.org/gaf/gene_association.ecocyc.gz)[108]. Further analysis
1136 was performed using custom MATLAB scripts, wherein the relative abundance of each
1137 protein was calculated for each sample and its replicates and then compared across
1138 conditions.
1139

1140 ***E. coli* transposon library temperature shifts**

1141 One milliliter of a pooled library of *E. coli* BW25113 transposon insertion mutants with
1142 random DNA barcodes[59] was thawed and diluted into 50 mL of LB+25 μg/mL
1143 kanamycin (Sigma Aldrich, St. Louis, MO) in a 250-mL Erlenmeyer flask (Pyrex,
1144 Glendale, AZ) and grown shaking overnight at 37 °C. 0.5 mL of the stationary-phase
1145 library cultures were diluted into 50 mL of LB in technical replicates at 25 °C and 37 °C.
1146

1147 The 25 °C culture was grown for 3 h to early log phase (OD_{600}~0.15) and 6 mL were
1148 diluted into in each of two flasks containing 50 mL fresh LB pre-warmed at 25 °C, then
1149 grown for another 3 h in an air-heated shaker (New Brunswick Scientific, Edison, NJ).
1150 The temperature upshift from 25 °C to 37 °C was performed by placing one of the 25 °C
1151 flasks into a heated water shaker at 37 °C. The control sample was left at 25 °C.
1152 Samples were collected in 1.5-mL aliquots and flash-frozen using liquid nitrogen every
1153 10 min at timepoints of -10, 0, 10, 20, 30, 40, 60, 90 min relative to the shift (control
1154 samples without temperature shifts were also taken at the same time points).
1155
1156 The 37 °C culture was grown for 2 h until mid- to late-log phase (OD_{600}~0.3) and 1.5 mL
1157 were diluted into each of two flasks containing 50 mL of fresh LB pre-warmed at 37 °C,
1158 then grown for ~1 h in a heated water shaker. For the temperature downshift from 37 °C
1159 to 25 °C, one of the flasks was first placed into a room-temperature water bath for 6 min
1160 for faster cooling, then transferred to an air-heated shaker at 25 °C. The other flask was
1161 maintained at 37 °C as a control.
1162
1163 Each set of downshift/upshift experiments was performed twice, and all samples were
1164 flash frozen and immediately stored at -80 °C. Optical density was monitored at each
1165 time point for all experiments with a Genesys 20 spectrophotometer (Thermo Fisher
1166 Scientific, Waltham, MA). The time scale of the temperature upshift was estimated to be
1167 ~3.5 min using a virtual experiment with 50 mL of water in a flask, whose temperature
1168 was directly monitored during a shift from 25 °C to 37 °C using the SiCTeC device
1169 thermistor reading. A similar test was performed for the 37 °C to 25 °C downshift by

1170 placing a 37 °C flask with 50 mL of water into a stationary water bath at room
1171 temperature, giving an estimate of ~6 min to complete the temperature shift.
1172
1173 ***E. coli* transposon mutant library sequencing and analysis**
1174 Barcode sequencing (BarSeq) was performed as previously described[59]. Briefly,
1175 genomic DNA was extracted using the DNeasy 96 Blood and Tissue kit (Qiagen) and
1176 quantified using the Quant-iT dsDNA BR Assay kit (Qiagen). BarSeq PCR was
1177 performed using 200 ng of genomic DNA template in 150-μL reaction volumes with Q5
1178 polymerase (with enhancer) (New England Biolabs, Ipswich, MA), 20 μM universal
1179 forward P5 primer, and 20 μM reverse P7 primers with 6-bp TruSeq indices that are
1180 automatically demultiplexed by Illumina software. PCR products were checked for
1181 completion using gel electrophoresis, and 10 μL of each reaction product were pooled
1182 and purified using the Zymo DNA Clean and Concentrator kit (Zymo Research, Irvine,
1183 CA). Sequencing was performed at the Chan Zuckerberg BioHub facility on an Illumina
1184 NextSeq 550 platform in High Output mode.
1185
1186 BarSeq analysis was performed as previously detailed[59], with relevant scripts at
1187 https://genomics.lbl.gov/supplemental/rbarseq/. Briefly, barcode reads were mapped to
1188 their corresponding genomic loci using sequencing of the transposon insertions in the *E.*
1189 *coli* library, and genes were filtered for those with ≥10 barcodes in the central (10–90%)
1190 portion of the gene. Temperature-shift samples were analyzed along with their
1191 corresponding unshifted control samples, with the time-zero sample corresponding to
1192 when the library was shifted (t=0 sample). The fitness of each mutant was measured as

1193 the $\log_2$ fold-change in its relative abundance, and further analysis was performed using
1194 custom MATLAB scripts.
1195

1196 **FRAP measurements**

1197 *E. coli* cultures were grown overnight from frozen stocks at 37 °C in LB, with 25 μg/mL
1198 kanamycin selection for Δ*fabR* and Δ*fadR* mutants, and then diluted 1:200 into fresh LB
1199 and grown until log phase at 37 °C (~2 h). Cultures were then diluted 1:10 into fresh LB,
1200 and 2 μL of 0.5 mg/mL MitoTracker Green (Thermo Fisher Scientific, Waltham, MA)
1201 were added. The culture was grown at the target temperature for 30 min to enable
1202 sufficient membrane labeling. Five hundred microliters of stained cells were washed via
1203 centrifugation (30 s at 7000 rcf) in fresh LB at the target temperature (37 °C or 27 °C).
1204 One microliter of washed culture was placed on an LB 3% agarose hydrogel and
1205 prepared for imaging using standard glass slide technique. Imaging was performed with
1206 a Zeiss LSM 880 confocal microscope with an environmental chamber for monitoring
1207 and controlling temperature (37 °C) and integrated with the ZEN software suite (Zeiss,
1208 Oberkochen, Germany). Temperature upshift experiments were performed by placing
1209 the sample into the heated environmental chamber for 5 min before imaging.
1210 Fluorescence recovery after photobleaching (FRAP) of individual cells was performed
1211 with excitation at 488 nm using the ZEN software by choosing a photobleaching region
1212 near cell tips covering 1/4 to 1/3 of the cell. The entire cell was imaged at minimum
1213 frame intervals (150–300 ms) to image fluorescence recovery.
1214

1215 **FRAP analysis and viscosity estimate**

1216 Individual regions of interest were manually delineated for the photobleached cell tips
1217 and the entire cell in FIJI[104], and the total fluorescence of each area was quantified at
1218 each time point. These data were imported for further analysis in MATLAB. The
1219 fluorescence recovery in each photobleached region was corrected by the rate of
1220 photobleaching in the entire cell, and the recovery curve was normalized and fit to the
1221 exponential function $(1 - e^{-\frac{t}{\tau_D}})$. The time constant (τ_D) was used to estimate a diffusion
1222 coefficient (D) via solution to Gaussian photobleaching in a plane, $\tau_D = \frac{r^2}{4D}$ (i.e.,
1223 modeling the cell tip as a disk of radius r on the membrane)[109]. The viscosity (η) was
1224 calculated using the Stokes-Einstein equation $(\eta = \frac{k_B T}{6\pi R D})$, where R is the radius of the
1225 fluorophore (estimated as 2 nm).
1226

1227 ***Schizosaccharomyces pombe* culturing**

1228 *S. pombe* WT972 h- was grown from a frozen stock on YE5S plates (5 g/L yeast
1229 extract, 30 g/L glucose, 225 mg/L each of adenine, histidine, leucine, uracil, and lysine
1230 hydrochloride, 2% Difco Bacto Agar). A single colony was grown at 22 °C or 32 °C in
1231 liquid YE5S overnight until saturation, then diluted 1:100 and grown until log phase
1232 (OD_{600}~0.3–0.5). One microliter of log-phase cells was placed on a 3% agarose YE5S
1233 pad at the initial temperature of the experiment for imaging.
1234

1235 **Estimate of LB molarity**

1236 LB is largely comprised of free amino acids, and measurements of *E. coli* auxotrophy
1237 and direct HPLC quantification[108] have provided an estimate of ~122 g/mol for its free
1238 amino acid content. The molar mass of tryptone is reported by the manufacturer to be

1239 71.08 g/mol (Thermo Fisher Scientific, Waltham, MA). As LB is composed of 10 g
1240 tryptone and 5 g yeast extract dissolved in 1 L H_2O, we estimate that the concentration
1241 of metabolizable free amino acids in LB is ~182 mM. Note that the accuracy of this
1242 estimate is not critical for any of our conclusions; the value simply enables plotting LB
1243 concentrations on the same plot as other substrates such as casamino acids.
1244

1245 **Measurements of K_M**

1246 *E. coli* MG1655 was grown overnight until saturation in MOPS buffer+0.2% (w/v)
1247 glucose at the target temperature (25 °C, 30 °C, 37 °C), then washed twice in MOPS
1248 buffer before being diluted 1:200 in the target medium at the target temperature. Liquid
1249 culture growth curves were obtained as described above. Optical density (OD) was
1250 measured using a microplate reader and maximal growth rate was quantified as the
1251 peak of the derivative of ln(background-subtracted OD)[98]. A weighted fit was performed
1252 on the growth rate versus concentration curve using the Monod equation (Eq. 4) to
1253 extract an estimate of K_M with a standard error. We note that it was challenging to
1254 obtain growth rates at low concentration for simple sugars (e.g., glucose, fructose), due
1255 to both the low K_M and generally low growth rate (<0.2 h^{-1}) (Fig. S13A–C). In succinate,
1256 the relationship between ln(growth rate) and 1/*T* appeared bilinear, thus a linear fit
1257 produced an estimate of E_a with very large standard error (19±14 kcal/mol) (Fig. S13G).

1258 **Figures**

1259

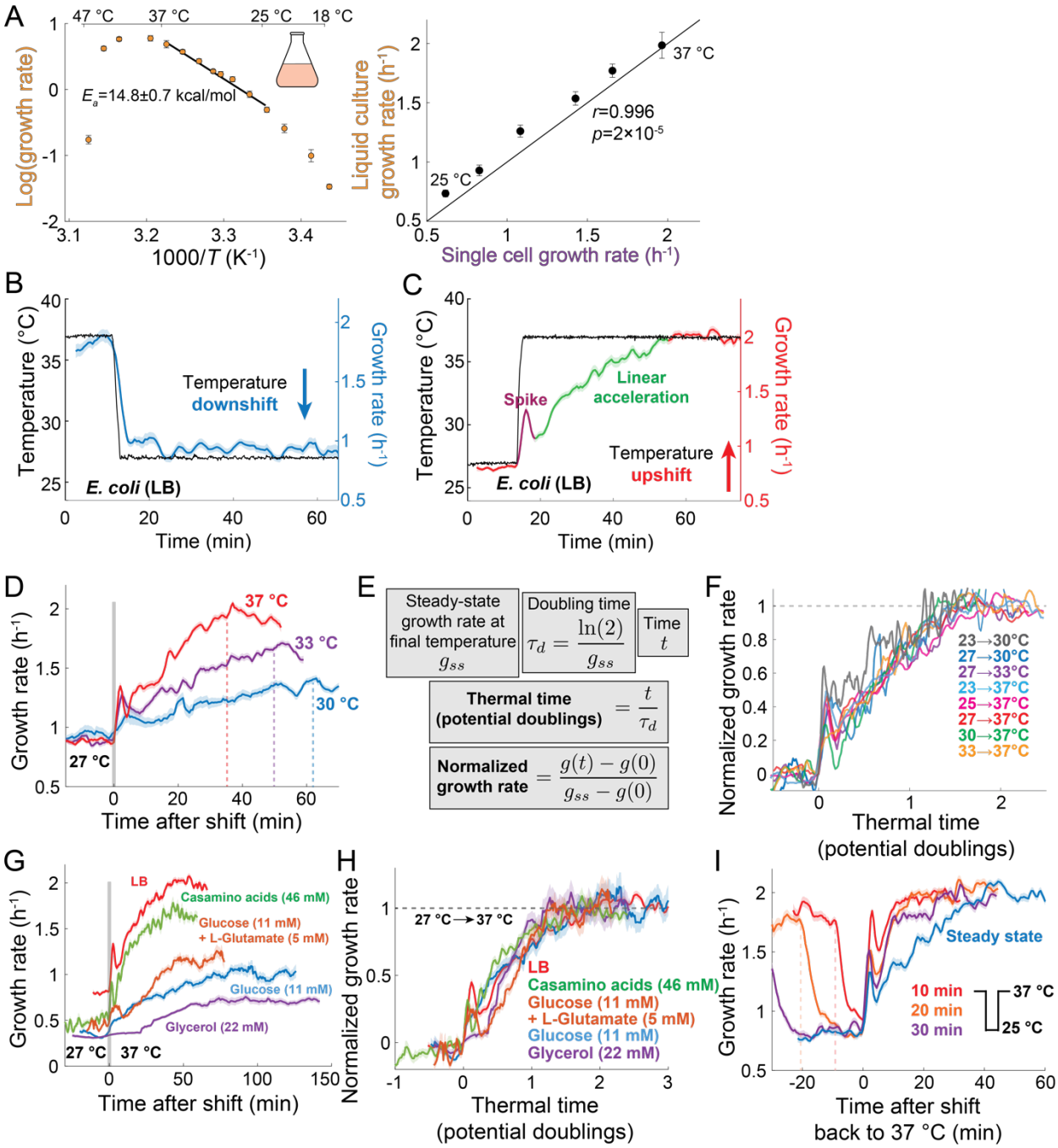

1260

1261 **Figure 1: *E. coli* responds asymmetrically to temperature shifts, and upshift**

1262 **dynamics are determined by the steady-state growth rate at the final temperature.**

1263 A) (Left) Arrhenius plot illustrating that the natural logarithm of *E. coli* MG1655
1264 maximal growth rate for temperatures between 25 °C and 37 °C varies linearly
1265 with the inverse absolute temperature, with a negative slope whose magnitude is
1266 the activation energy (E_a). (Right) Liquid-culture and single-cell growth rates were
1267 highly correlated for temperatures in the Arrhenius range between 25 °C and
1268 37 °C (data from Fig. S1C,E).
1269 B) Single-cell growth rate (blue) of *E. coli* MG1655 throughout a temperature (black)
1270 downshift from 37 °C to 27 °C in rich growth medium (LB) (n=253 cells). The
1271 curve is the mean growth rate and the shaded region represents one standard
1272 error of the mean (SEM) Growth rate responds quickly to the downshift.
1273 C) Single-cell growth rate (red) of *E. coli* MG1655 throughout a temperature (black)
1274 upshift from 27 °C to 37 °C in LB (n=792 cells). The curve is the mean growth
1275 rate and the shaded regions represent ±1 SEM. Growth rate initially spikes (dark
1276 red), followed by linear acceleration (green) to the new steady-state value over
1277 ~35 min.
1278 D) Single-cell growth rate of *E. coli* MG1655 throughout a temperature upshift from
1279 27 °C to 30 °C (blue, n=253 cells), 33 °C (purple, n=754 cells), or 37 °C (red,
1280 n=904 cells) in LB. Vertical dashed lines indicate the time at which the growth
1281 rate reached its steady-state value at the higher temperature. Curves show the
1282 mean growth rate and the shaded regions represent ±1 SEM.
1283 E) The thermal time is defined as the time (t) measured in units of doubling times
1284 (τ_d) of steady-state growth at the higher temperature. The normalized growth rate
1285 is defined as the difference between the growth rate at time ($g(t)$) and the growth

1286 rate at the temperature shift ($g(0)$) divided by the difference between the steady-
1287 state growth rate at the higher temperature (g_{ss}) and the initial temperature ($g(0)$).
1288 F) Normalized single-cell growth rate of *E. coli* MG1655 grown in LB exhibits a
1289 characteristic response with respect to thermal time for shifts between two
1290 temperatures in the Arrhenius range 23 °C–37 °C (n=253–904 cells). Curves
1291 represent the mean, and error bars have been omitted for ease of viewing.
1292 G) Single-cell growth rate of *E. coli* MG1655 throughout a temperature upshift from
1293 27 °C to 37 °C in LB (red, n=792 cells), casamino acids (green, n=270 cells),
1294 glucose (blue, n=353 cells), glucose+glutamate (orange, n=220 cells), or glycerol
1295 (purple, n=520 cells). Curves show the mean growth rate and the shaded regions
1296 represent ±1 SEM.
1297 H) Despite the wide variation in absolute growth-rate responses (G), normalized
1298 growth rate followed an approximately conserved trajectory versus thermal time
1299 across nutrient environments.
1300 I) Single-cell growth rates of *E. coli* MG1655 in LB grown to steady state at 37 °C
1301 and then subjected to pulses at 25 °C for 10 min (red, n=1015 cells), 20 min
1302 (orange, n=1022 cells), or 30 min (purple, n=586 cells). Vertical dotted lines
1303 represent the times at which cells were subjected to the downshift to 25 °C for
1304 the 10- and 20-min pulses. The upshift from steady-state growth at 25 °C to
1305 37 °C is also shown for comparison (blue, n=773 cells). Curves show the mean
1306 growth rate and the shaded regions represent ±1 SEM.

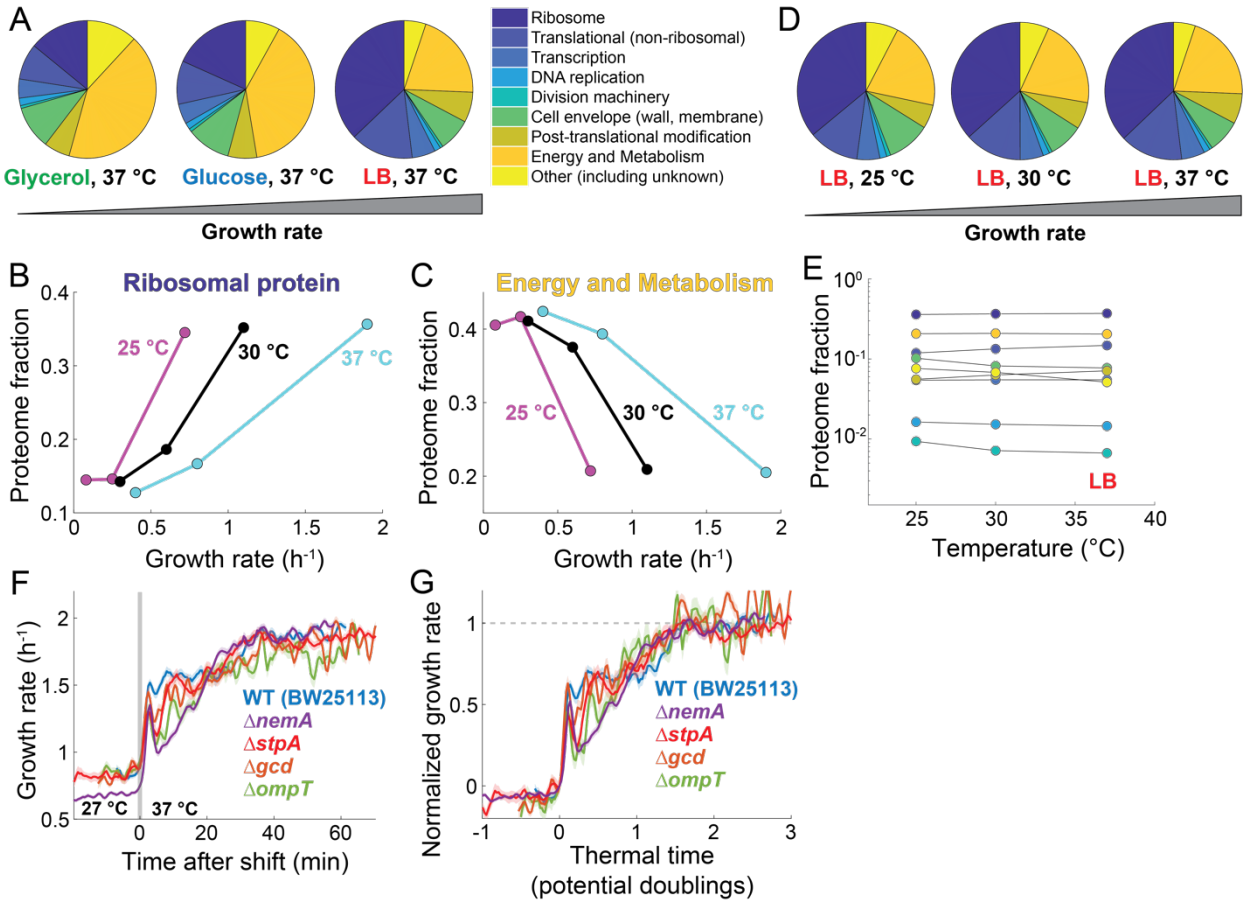

Figure 2: The delayed response to a temperature upshift is not due to proteome rearrangement.

A) The *E. coli* proteome at 37 °C varies across media. Functional proteomic sectors (pie chart) were annotated according to the Clusters of Orthologous Groups (COG) classification (Methods).

B) Ribosomal protein fraction increased with growth rate across media (M9+glycerol, M9+glucose, LB), independent of growth temperature.

C) Energy and metabolism protein fraction decreased with growth rate across media (M9+glycerol, M9+glucose, LB), independent of growth temperature.

D) The *E. coli* proteome in LB is largely invariant across temperatures in the Arrhenius range (25 °C–37 °C).

1319 E) The proteome fraction accounted for by each functional category was
1320 approximately constant in LB across Arrhenius temperatures. Colors correspond
1321 to the functions in the legend in (A).
1322 F) Temperature-upshift (27 °C to 37 °C) responses of individual deletion mutants of
1323 the four most abundant of the proteins whose relative abundance scaled with
1324 temperature across all media conditions. (blue: parent strain wild-type BW25113,
1325 *n*=710 cells; purple: Δ*nemA*, *n*=1052 cells; red: Δ*stpA*, *n*=588 cells; orange: Δ*gcd*,
1326 *n*=814 cells; green: Δ*ompT*, *n*=324 cells). Curves show the mean growth rate and
1327 the shaded regions represent ±1 SEM.
1328 G) Normalized growth rate followed an approximately conserved trajectory versus
1329 thermal time across the mutant growth data in (F).

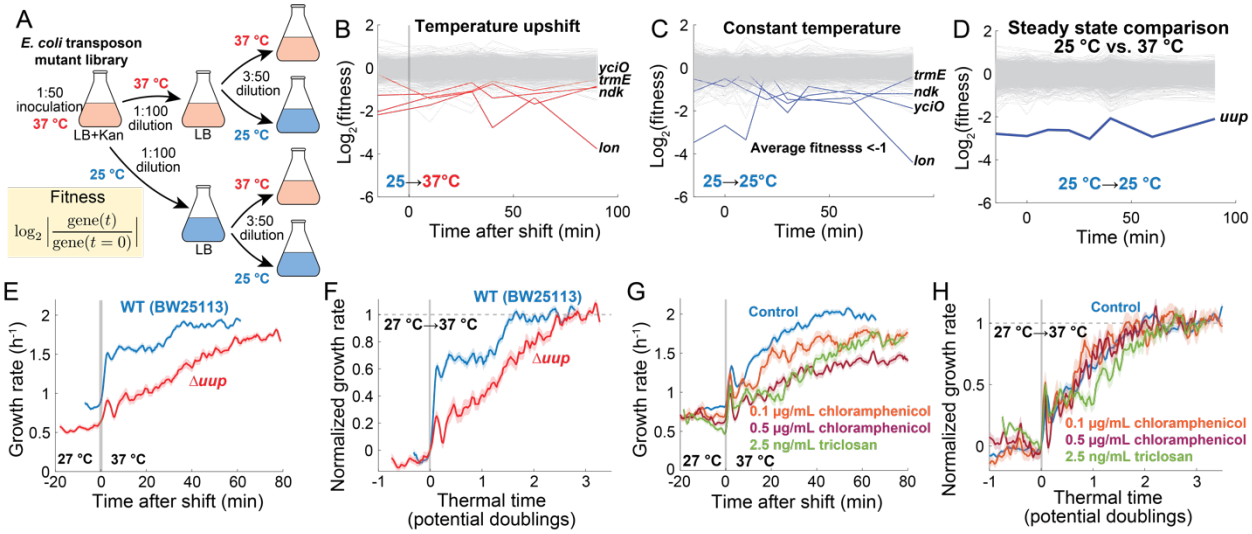

Figure 3: Response time is unaffected by almost all genetic and chemical perturbations.

A) Schematic of temperature-shift experiments screening a pooled library of *E. coli* BW25113 randomly barcoded transposon mutants (Methods). The library was initially grown in a 50-mL volume at 37 °C, then diluted and grown to steady state at the initial target temperature (25 °C or 37 °C) before shifting to 25 °C or 37 °C at time *t*=0. The optical density was monitored at each sampling time point (~10 min intervals). The fitness of each mutant is defined as the $\log_2$(relative abundance compared to *t*=0) (Methods). This experiment was carried out twice.

B) Trajectories of mutant fitness during a shift from 25 °C to 37 °C (gray vertical bar denotes timing of the shift). Mutants with fitness<-1 when averaged over time points are highlighted in red.

C) Trajectories of mutant fitness during steady-state growth at 25 °C. Mutants with fitness<-1 when averaged over time points are highlighted in blue. (B) and (C) are from the same experiment, and outlier mutants in the upshift (B) were also outliers in the control (C).

1347 D) Trajectories of $\log_2$(relative abundance) during steady-state growth at 25 °C
1348 compared with at 37 °C. A single gene, *uup*, had fitness<-1 when averaged over
1349 time points.
1350 E) Single-cell growth rate of Δ*uup* (red, *n*=609 cells) and its parent BW25113 (blue,
1351 *n*=734 cells) throughout a temperature shift from 27 °C to 37 °C. Curves show
1352 the mean growth rate and shaded regions represent ±1 SEM.
1353 F) Normalized growth rate versus thermal time for each trajectory in (E) shows that
1354 Δ*uup* cells respond more slowly to an upshift.
1355 G) Single-cell growth rates of *E. coli* MG1655 in LB treated with 0.1 μg/mL
1356 chloramphenicol (orange, *n*=264 cells), 0.5 μg/mL chloramphenicol (dark red,
1357 *n*=382 cells) or 2.5 ng/mL triclosan (green, *n*=266 cells) throughout a shift from
1358 27 °C to 37 °C. The untreated control is also shown for comparison (blue, *n*=792
1359 cells). Curves show the mean growth rate and shaded regions represent ±1
1360 SEM.
1361 H) Normalized growth rate followed a similar trajectory versus thermal time as the
1362 control for the chloramphenicol treatment data in (G), while triclosan slightly
1363 delayed the growth-rate response.

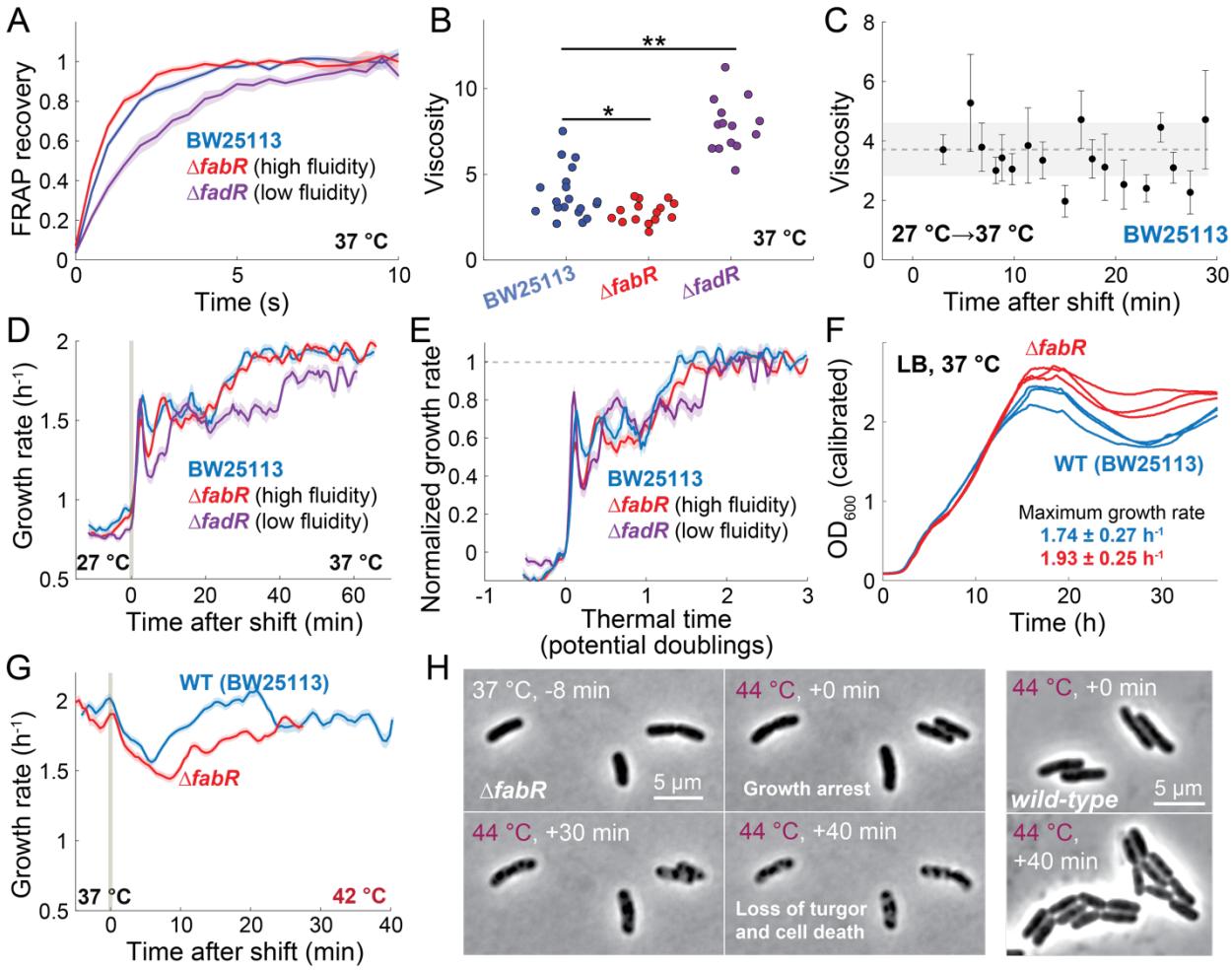

Figure 4: Changes in membrane fluidity do not alter the response to temperature upshift but increase lysis at high temperatures.

A) FRAP recovery dynamics of the membrane dye MitoTracker in the parent strain BW25113 (blue, *n*=19 cells), the high-fluidity mutant Δ*fabR* (red, *n*=15 cells), and the low-fluidity mutant Δ*fadR* (purple, *n*=14 cells) grown on LB (Methods). Curves show the mean recovery and shaded regions represent ±1 SEM.

B) Membrane viscosity (Methods) was significantly lower and higher in Δ*fabR* and Δ*fadR*, respectively, compared with the parent. Significance was determined using a two-sample t-test; *: $p<0.05$, **: $p<0.005$.

1374 C) Membrane viscosity of *E. coli* BW25113 cells after an upshift at *t*=0 from 27 °C to
1375 37 °C in LB (Methods). Points are estimates from a best fit (Methods) and error
1376 bars represent 1 standard error. Dotted line is the mean viscosity from steady-
1377 state measurements (B), and the shaded region represents ±1 standard
1378 deviation.
1379 D) Growth rate responses of *E. coli* BW25113 (blue, *n*=686 cells), Δ*fabR* (red,
1380 *n*=924 cells), and Δ*fadR* (purple, *n*=409 cells) to a temperature upshift from 27 °C
1381 to 37 °C in LB. Curves show mean growth rate and shaded regions represent ±1
1382 SEM.
1383 E) Normalized growth rate followed a similar trajectory versus thermal time among
1384 the mutants and parent for the data in (D).
1385 F) Growth curves of wild-type (BW25113) (blue) and Δ*fabR* (red) cells grown in LB
1386 at 37 °C (*n*=3 replicates). Optical density (OD) was corrected for non-linearity at
1387 high OD values (Methods). Maximum growth rates are the mean across
1388 replicates and the error is ±1 standard deviation.
1389 G) Growth rate response to a temperature upshift from 37 °C to 42 °C in *E. coli*
1390 BW25113 (blue, *n*=1011 cells) and Δ*fabR* (red, *n*=554 cells). Both strains
1391 exhibited an initial decrease in growth rate followed by recovery to the steady-
1392 state growth rate at 37 °C, but recovery was more delayed for the high-fluidity
1393 Δ*fabR* mutant. Curves show mean growth rate and shaded regions represent ±1
1394 SEM.
1395 H) (Left) Representative images of Δ*fabR* cells throughout a temperature upshift
1396 from 37 °C to 44 °C. At 37 °C, morphology and growth were wild-type-like (top

1397 left). Growth halted immediately after the shift to 44 °C (top right), with loss of
1398 turgor and cell death occurring within 30–40 min after the shift (bottom left, right).
1399 (Right) Representative images of wild-type MG1655 cells before and after an
1400 upshift from 37 °C to 44 °C. Cells maintained growth and shape.

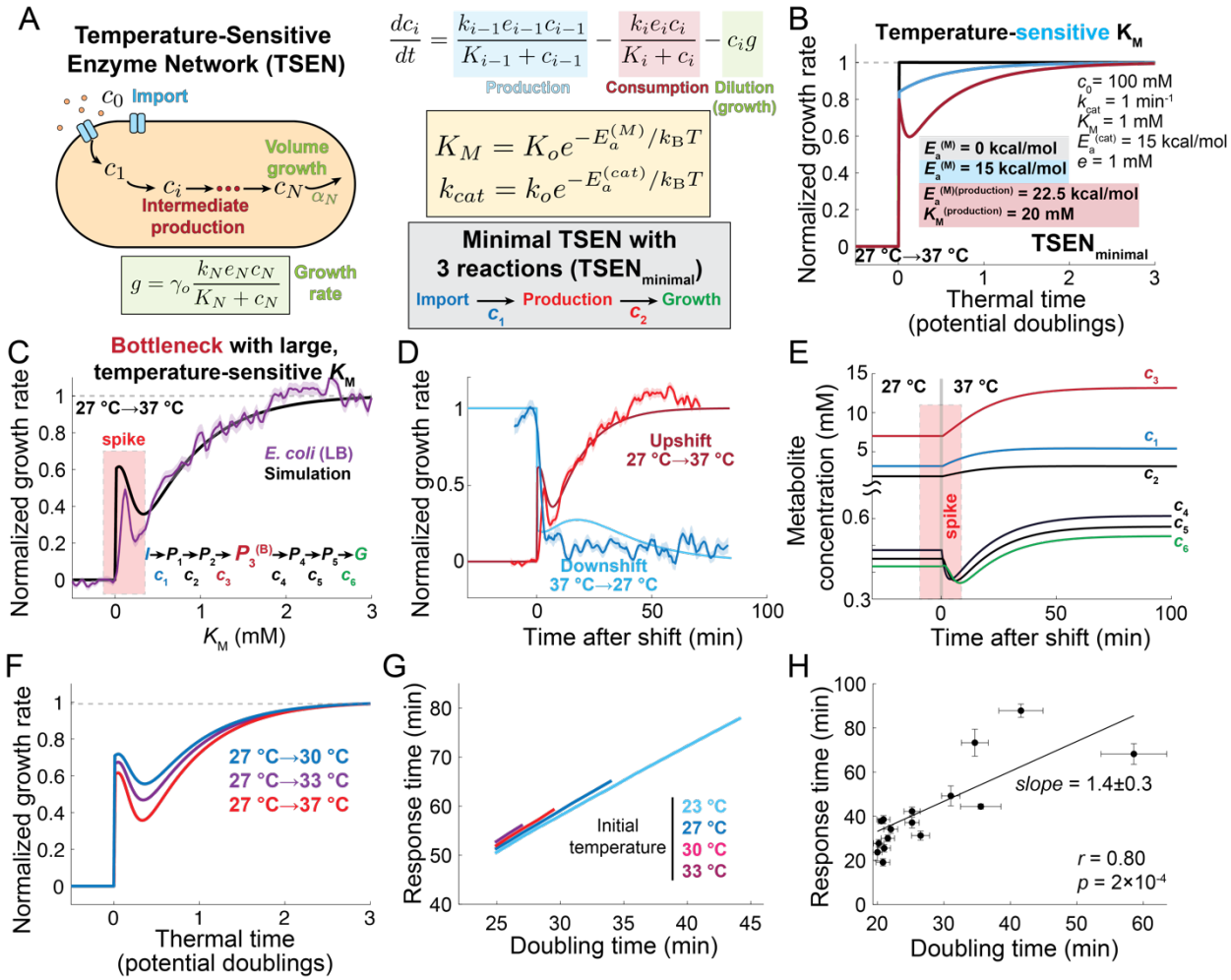

Figure 5: A temperature-sensitive enzyme network (TSEN) model recapitulates temperature-shift behaviors through metabolome rearrangement.

A) (Upper left) In the TSEN model, the import reaction (blue), production reactions (dark red), and volume growth reaction (green) are chained Michaelis-Menten reactions. (Upper right) The rate equation for each intermediate metabolite (c_i) involves enzymatic production from c_{i-1} by enzyme e_{i-1} (blue), enzymatic consumption by enzyme e_i (red), and dilution by volume growth g (green). The final intermediate c_N is translated into volume growth with an efficiency factor γ_0 (green box). Each kinetic parameter is assumed to be temperature sensitive

1411 according to an Arrhenius equation with activation energy E_a (yellow box). A
1412 minimal TSEN model ($TSEN_{minimal}$) has a single intermediate production reaction
1413 (red), such that the network has only 2 intermediate metabolites (c_1, c_2; gray
1414 box).

1415 B) Normalized growth rate versus thermal time from simulations of a minimal TSEN
1416 model with (blue) and without (black) a temperature-sensitive Michaelis-Menten
1417 constant (K_M) throughout a temperature shift from 27 °C to 37 °C. All other model
1418 parameters are identical and are defined in the panel inset. The TSEN with a
1419 temperature-sensitive K_M results in a non-zero response time (blue). A TSEN
1420 model with a bottleneck (dark red, $K_M = 20$ mM, $E_a = 22.5$ kcal/mol) produces an
1421 initial spike.

1422 C) A TSEN model with a single bottleneck (red, P_3) embedded within a 7-reaction
1423 chain produces a quantitatively similar response to an upshift from 27 °C to 37 °C
1424 as *E. coli* MG1655 cells on LB (purple, *n*=792 cells; shaded region represents ±1
1425 SEM). All other reactions have parameters identical to the minimal model without
1426 a bottleneck (blue) in (B).

1427 D) Normalized growth rate in simulations of the bottlenecked TSEN model in (C)
1428 throughout an upshift (dark red) or downshift (light blue) between 27 °C and
1429 37 °C. In contrast to the spike and slow response to the upshift, the downshift
1430 results in immediate deceleration to a growth rate close to the steady-state value
1431 at 27 °C, followed by slow deceleration to new steady-state value. Overlaid are
1432 the normalized growth rates of *E. coli* MG1655 subjected to an upshift (red, 27 °C

1433 to 37 °C, n=792 cells) or downshift (blue, 37 °C to 27 °C, n=253 cells). Shaded
1434 error bars represent ±1 SEM.

1435 E) The TSEN model in (C) predicts that metabolites upstream of the bottleneck
1436 ($c_{1,2,3}$) will have lower concentrations than those after the bottleneck ($c_{4,5,6}$) and
1437 increase slowly on the time scale of growth after an upshift. Post-bottleneck
1438 metabolites undergo transient decreases immediately after the temperature
1439 upshift over a time interval corresponding to the spike (red box). After this initial
1440 period, all metabolites increase to new values corresponding to the steady state
1441 at the higher temperature.

1442 F) The TSEN model in (C) predicts highly similar responses of normalized growth
1443 rate with thermal time for upshifts from 27 °C to 30 °C (blue), 33 °C (purple), or
1444 37 °C (red).

1445 G) Over a broad range of final temperatures, the absolute upshift response time
1446 (time to reach 98% of the difference between steady-state growth rates) has
1447 linear scaling with the doubling time at the final temperature. Each line
1448 represents simulations from a given initial temperature to temperatures up to
1449 37 °C.

1450 H) Experimental estimates of absolute response time follow a linear scaling with
1451 doubling time at the final temperature, similar to simulations in (G). Shown are
1452 data for upshifts involving initial and final temperatures ranging between 23 °C
1453 and 37 °C (data from Fig. 1F–H).

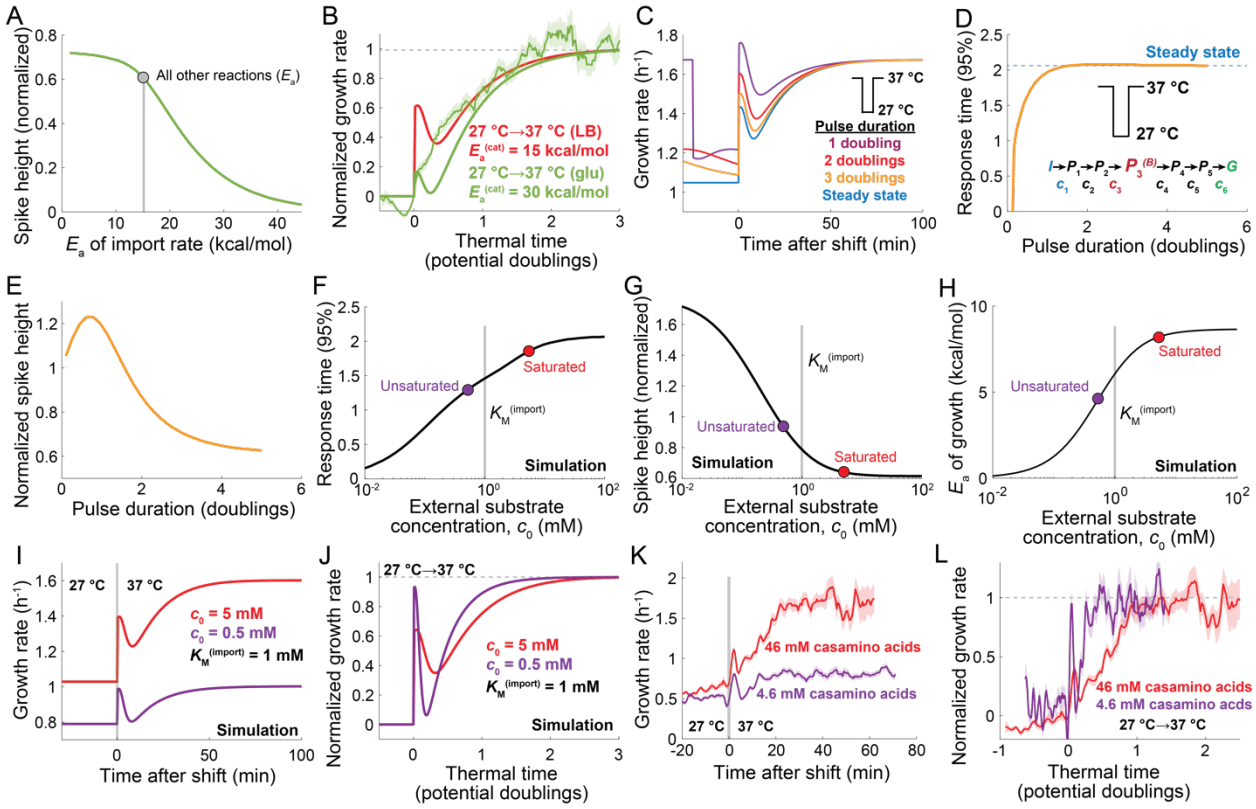

Figure 6: TSEN model predicts changes to upshift response during growth on simple sugars, after a downshift pulse, and at low nutrient concentration.

A) The bottlenecked TSEN model in Fig. 5C predicts that spike height after a temperature upshift will decrease with the activation energy of import. The activation energies of all other reactions were set to 15 kcal/mol (gray circle).

B) Increasing the activation energy of import to $E_a = 30\ \mathrm{kcal/mol}$ based on our experimental measurements of the activation energy of growth in glucose (Fig. S12G) dramatically reduced the spike height (green) compared with our default $E_a = 15\ \mathrm{kcal/mol}$ (red) without affecting the response time, similar to our experimental measurements of the normalized growth-rate response on glucose (green data, same as in Fig. 1H).

1466 C) The bottlenecked TSEN model predicts that short downshift pulses from 37 °C to
1467 27 °C (purple, red, orange) will cause larger spikes and faster recovery to the
1468 steady-state growth rate at 37 °C than an upshift from steady state at 27 °C to
1469 37 °C (blue), similar to our experimental observations (Fig. 1I).
1470 D,E) The bottlenecked TSEN model in Fig. 5C predicts that the response time
1471 decreases for downshift pulses of duration <1 doubling at the higher temperature
1472 (D) and that the spike height remains high for pulses of duration multiple
1473 doublings at the higher temperature (E).
1474 F,G,H) The bottlenecked TSEN model in Fig. 5C predicts that response time
1475 decreases (F), spike height increases (G), and growth activation energy
1476 decreases (H) when nutrient concentration is reduced from above (saturated, red
1477 circle) to below (unsaturated, purple circle) the K_M for import (gray vertical bar).
1478 I) Simulations of the bottlenecked TSEN model in Fig. 5C throughout an upshift
1479 from 27 °C to 37 °C for high (c_0=5 mM, red) or low (c_0=0.5 mM, purple) external
1480 substrate concentration ($K_M^{(import)}$ = 1 mM). The absolute spike height is similar in
1481 magnitude at both concentrations, but the steady-state growth rate at 37 °C is
1482 much lower for lower external substrate concentration (purple) and is reached
1483 more quickly after the upshift than for higher concentration (red).
1484 J) The normalized growth rate calculated from simulations in (H) has a larger spike
1485 and a faster normalized response (<1 doubling) for low external substrate
1486 concentration (purple) compared with the TSEN model at saturation (red).
1487 K,L) Growth rate throughout an upshift from 27 °C to 37 °C of *E. coli* MG1655 grown
1488 on MOPS+46 mM casamino acids (red, *n*=116 cells) or 4.6 mM casamino acids

(purple, *n*=261 cells) exhibits similar dynamics in both absolute (J) and normalized (K) terms as the simulations in (H,I). Curves are mean growth rate and shaded regions represent ±1 SEM. The response time at low casamino acid concentration is much shorter (purple, ~0.25 doublings) compared to at saturation (red, ~1.4 doublings) and is accompanied by a larger relative spike height.

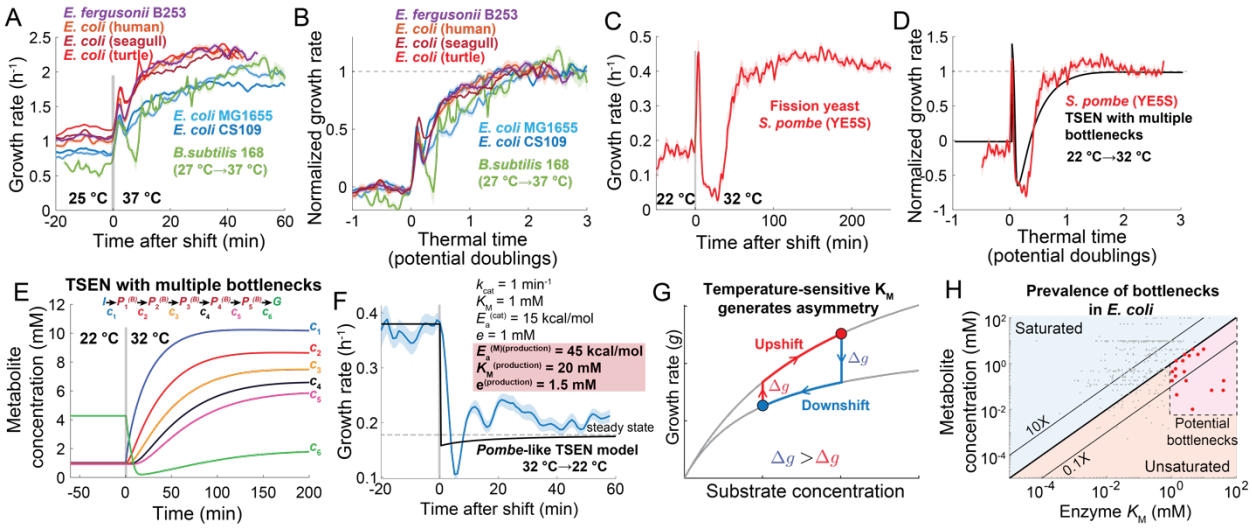

Figure 7: Temperature upshift response features are generally conserved across microbes and can be captured by the TSEN model.

A) Growth-rate response to a temperature upshift on LB of laboratory-evolved *E. coli* (light and dark blue, *n*=773–1279 cells) and natural isolates from various hosts (orange to red, *n*=389–547 cells), *Escherichia fergusonii* (purple, *n*=997 cells), and *Bacillus subtilis* (green, *n*=236 cells). All upshifts were from 25 °C to 37 °C, except for *B. subtilis* (27 °C to 37 °C). Curves are mean growth rate and shaded regions represent ±1 SEM.

B) Normalized growth rate followed a similar trajectory versus thermal time across all strains/species for the data in (A).

C) A temperature upshift from 22 °C to 32 °C on the rich growth medium YE5S caused the growth rate of the fission yeast *Schizosaccharomyces pombe* to initially spike to close to the steady-state value at 32 °C, then decelerate to below the steady-state value at 22 °C, then accelerate back to the new steady-state value within less than a doubling (~100 min) (red, *n*=333 cells). Curves are mean growth rate and shaded regions represent ±1 SEM.

D) A TSEN model with 5 intermediate reactions, each with a large (20 mM) and highly temperature-sensitive K_M ($E_a^{(M)} = 22.5\ \mathrm{kcal/mol}$) produces similar normalized growth rate dynamics with thermal time (black) as the *S. pombe* data in (C) (red), characterized by a large spike, deceleration to <0, and fast recovery within <1 doubling.

E) The TSEN model in (D), composed entirely of bottlenecks, predicts that a temperature upshift results in a rapid, large decrease in the final intermediate metabolite concentration (c_6), followed by a slower increase to the new steady-state, which is lower than at lower temperature. All other metabolite concentrations (c_{1-5}) increase monotonically toward their steady-state levels at rates that depend inversely on their network depth (i.e., c_5 increases more slowly than c_1).

F) An extended TSEN model with five intermediate reactions, each with a large (20 mM) and highly temperature-sensitive (E_a=22.5 kcal/mol) K_M, predicts a temporary undershoot (black) upon a downshift to growth rates below the steady state value at the lower temperature. The fission yeast *Schizosaccharomyces pombe* exhibited an undershoot during a downshift from 32 °C to 32 °C on rich medium (YE5S) (blue, *n*=54 cells) similar to model predictions. Experimental data are the mean±1 SEM (shaded region) at each time point.

G) Asymmetry in growth-rate response to temperature up- and downshifts is caused by the temperature sensitivity of K_M. If substrate concentration is near the K_M and $E_a^{(M)} > 0$, an upshift causes a small initial increase in growth rate, followed by a slow increase in substrate concentration to the new K_M via production (red).

1535 Conversely, a downshift causes a comparatively larger initial decrease in growth
1536 rate, followed by a slow decrease in substrate concentration to the new K_M via
1537 dilution (blue).
1538 H) Intracellular metabolite concentrations are generally much higher than the K_M of
1539 their production enzyme for *E. coli* grown on glucose (data from Ref. [81]).
1540 However, some metabolites have concentrations near or below the K_M of their
1541 production, and potential bottlenecks (purple region, red points) are those with
1542 K_M>1 mM and substrate concentration $c<K_M$.

1543 **BIBLIOGRAPHY**

1544

1545 1. Kanjee, U., and Houry, W.A. (2013). Mechanisms of acid resistance in
1546 Escherichia coli. Annu Rev Microbiol *67*, 65-81. 10.1146/annurev-micro-092412-
1547 155708.

1548 2. Sleator, R.D., and Hill, C. (2002). Bacterial osmoadaptation: the role of osmolytes
1549 in bacterial stress and virulence. FEMS Microbiol Rev *26*, 49-71. 10.1111/j.1574-
1550 6976.2002.tb00598.x.

1551 3. Rojas, E., Theriot, J.A., and Huang, K.C. (2014). Response of Escherichia coli
1552 growth rate to osmotic shock. Proc Natl Acad Sci U S A *111*, 7807-7812.
1553 10.1073/pnas.1402591111.

1554 4. Dai, X., Zhu, M., Warren, M., Balakrishnan, R., Patsalo, V., Okano, H.,
1555 Williamson, J.R., Fredrick, K., Wang, Y.P., and Hwa, T. (2016). Reduction of
1556 translating ribosomes enables Escherichia coli to maintain elongation rates
1557 during slow growth. Nat Microbiol *2*, 16231. 10.1038/nmicrobiol.2016.231.

1558 5. Sunagawa, S., Coelho, L.P., Chaffron, S., Kultima, J.R., Labadie, K., Salazar, G.,
1559 Djahanschiri, B., Zeller, G., Mende, D.R., Alberti, A., et al. (2015). Ocean
1560 plankton. Structure and function of the global ocean microbiome. Science *348*,
1561 1261359. 10.1126/science.1261359.

1562 6. Melillo, J.M., Frey, S.D., DeAngelis, K.M., Werner, W.J., Bernard, M.J., Bowles,
1563 F.P., Pold, G., Knorr, M.A., and Grandy, A.S. (2017). Long-term pattern and
1564 magnitude of soil carbon feedback to the climate system in a warming world.
1565 Science *358*, 101-105. 10.1126/science.aan2874.

1566 7. Zhang, Y., and Gross, C.A. (2021). Cold Shock Response in Bacteria. Annu Rev
1567 Genet *55*, 377-400. 10.1146/annurev-genet-071819-031654.
1568 8. Richter, K., Haslbeck, M., and Buchner, J. (2010). The heat shock response: life
1569 on the verge of death. Mol Cell *40*, 253-266. 10.1016/j.molcel.2010.10.006.
1570 9. Barber, M.A. (1908). The Rate of Multiplication of Bacillus Coli at Different
1571 Temperatures. The Journal of Infectious Diseases *5*, 379-400.
1572 10.1093/infdis/5.4.379.
1573 10. Mohr, P.W., and Krawiec, S. (1980). Temperature characteristics and Arrhenius
1574 plots for nominal psychrophiles, mesophiles and thermophiles. J Gen Microbiol
1575 *121*, 311-317. 10.1099/00221287-121-2-311.
1576 11. Herendeen, S.L., VanBogelen, R.A., and Neidhardt, F.C. (1979). Levels of major
1577 proteins of Escherichia coli during growth at different temperatures. J Bacteriol
1578 *139*, 185-194. 10.1128/jb.139.1.185-194.1979.
1579 12. Knapp, B.D., and Huang, K.C. (2022). The Effects of Temperature on Cellular
1580 Physiology. Annu Rev Biophys *51*, 499-526. 10.1146/annurev-biophys-112221-
1581 074832.
1582 13. Elias, M., Wieczorek, G., Rosenne, S., and Tawfik, D.S. (2014). The universality
1583 of enzymatic rate-temperature dependency. Trends Biochem Sci *39*, 1-7.
1584 10.1016/j.tibs.2013.11.001.
1585 14. Dill, K.A., Ghosh, K., and Schmit, J.D. (2011). Physical limits of cells and
1586 proteomes. Proc Natl Acad Sci U S A *108*, 17876-17882.
1587 10.1073/pnas.1114477108.

1588 15. Nguyen, V., Wilson, C., Hoemberger, M., Stiller, J.B., Agafonov, R.V., Kutter, S.,
1589 English, J., Theobald, D.L., and Kern, D. (2017). Evolutionary drivers of
1590 thermoadaptation in enzyme catalysis. Science *355*, 289-294.
1591 10.1126/science.aah3717.
1592 16. Chen, K., Gao, Y., Mih, N., O'Brien, E.J., Yang, L., and Palsson, B.O. (2017).
1593 Thermosensitivity of growth is determined by chaperone-mediated proteome
1594 reallocation. Proc Natl Acad Sci U S A *114*, 11548-11553.
1595 10.1073/pnas.1705524114.
1596 17. Phillips, R., Kondev, J., and Theriot, J. (2009). Physical Biology of the Cell
1597 (Garland Science).
1598 18. Hinshelwood, C.N. (1952). On the chemical kinetics of autosynthetic systems.
1599 Journal of the Chemical Society (Resumed), 745-755. 10.1039/JR9520000745.
1600 19. Iyer-Biswas, S., Wright, C.S., Henry, J.T., Lo, K., Burov, S., Lin, Y., Crooks, G.E.,
1601 Crosson, S., Dinner, A.R., and Scherer, N.F. (2014). Scaling laws governing
1602 stochastic growth and division of single bacterial cells. Proc Natl Acad Sci U S A
1603 *111*, 15912-15917. 10.1073/pnas.1403232111.
1604 20. Farewell, A., and Neidhardt, F.C. (1998). Effect of temperature on in vivo protein
1605 synthetic capacity in Escherichia coli. J Bacteriol *180*, 4704-4710.
1606 10.1128/JB.180.17.4704-4710.1998.
1607 21. Chohji, T., Sawada, T., and Kuno, S. (1983). Effects of temperature shift on
1608 growth rate of Escherichia coli BB at lower glucose concentration. Biotechnol
1609 Bioeng *25*, 2991-3003. 10.1002/bit.260251215.

1610 22. Lemaux, P.G., Herendeen, S.L., Bloch, P.L., and Neidhardt, F.C. (1978).
1611 Transient rates of synthesis of individual polypeptides in E. coli following
1612 temperature shifts. Cell *13*, 427-434. 10.1016/0092-8674(78)90317-3.
1613 23. Gadgil, M., Kapur, V., and Hu, W.S. (2005). Transcriptional response of
1614 Escherichia coli to temperature shift. Biotechnol Prog *21*, 689-699.
1615 10.1021/bp049630l.
1616 24. Tagkopoulos, I., Liu, Y.C., and Tavazoie, S. (2008). Predictive behavior within
1617 microbial genetic networks. Science *320*, 1313-1317. 10.1126/science.1154456.
1618 25. Zhou, Y.N., Kusukawa, N., Erickson, J.W., Gross, C.A., and Yura, T. (1988).
1619 Isolation and characterization of Escherichia coli mutants that lack the heat shock
1620 sigma factor sigma 32. J Bacteriol *170*, 3640-3649. 10.1128/jb.170.8.3640-
1621 3649.1988.
1622 26. Sinensky, M. (1974). Homeoviscous adaptation--a homeostatic process that
1623 regulates the viscosity of membrane lipids in Escherichia coli. Proc Natl Acad Sci
1624 U S A *71*, 522-525. 10.1073/pnas.71.2.522.
1625 27. Budin, I., de Rond, T., Chen, Y., Chan, L.J.G., Petzold, C.J., and Keasling, J.D.
1626 (2018). Viscous control of cellular respiration by membrane lipid composition.
1627 Science *362*, 1186-1189. 10.1126/science.aat7925.
1628 28. Scott, M., Klumpp, S., Mateescu, E.M., and Hwa, T. (2014). Emergence of robust
1629 growth laws from optimal regulation of ribosome synthesis. Mol Syst Biol *10*, 747.
1630 10.15252/msb.20145379.

1631 29. Bremer, H., and Dennis, P.P. (2008). Modulation of Chemical Composition and
1632 Other Parameters of the Cell at Different Exponential Growth Rates. EcoSal Plus
1633 *3*. 10.1128/ecosal.5.2.3.
1634 30. Belliveau, N.M., Chure, G., Hueschen, C.L., Garcia, H.G., Kondev, J., Fisher,
1635 D.S., Theriot, J.A., and Phillips, R. (2021). Fundamental limits on the rate of
1636 bacterial growth and their influence on proteomic composition. Cell Syst *12*, 924-
1637 944 e922. 10.1016/j.cels.2021.06.002.
1638 31. Zaritsky, A. (1982). Effects of growth temperature on ribosomes and other
1639 physiological properties of Escherichia coli. J Bacteriol *151*, 485-486.
1640 10.1128/jb.151.1.485-486.1982.
1641 32. Ram, J.L., Ritchie, R.P., Fang, J., Gonzales, F.S., and Selegean, J.P. (2004).
1642 Sequence-based source tracking of Escherichia coli based on genetic diversity of
1643 beta-glucuronidase. J Environ Qual *33*, 1024-1032. 10.2134/jeq2004.1024.
1644 33. Ram, J.L., Thompson, B., Turner, C., Nechvatal, J.M., Sheehan, H., and Bobrin,
1645 J. (2007). Identification of pets and raccoons as sources of bacterial
1646 contamination of urban storm sewers using a sequence-based bacterial source
1647 tracking method. Water Res *41*, 3605-3614. 10.1016/j.watres.2007.04.013.
1648 34. Soupene, E., van Heeswijk, W.C., Plumbridge, J., Stewart, V., Bertenthal, D.,
1649 Lee, H., Prasad, G., Paliy, O., Charernnoppakul, P., and Kustu, S. (2003).
1650 Physiological studies of Escherichia coli strain MG1655: growth defects and
1651 apparent cross-regulation of gene expression. J Bacteriol *185*, 5611-5626.
1652 10.1128/JB.185.18.5611-5626.2003.

1653 35. Eydallin, G., Ryall, B., Maharjan, R., and Ferenci, T. (2014). The nature of
1654 laboratory domestication changes in freshly isolated Escherichia coli strains.
1655 Environ Microbiol *16*, 813-828. 10.1111/1462-2920.12208.
1656 36. Bronikowski, A.M., Bennett, A.F., and Lenski, R.E. (2001). Evolutionary
1657 adaptation to temperature. VIII. Effects of temperature on growth rate in natural
1658 isolates of Escherichia coli and Salmonella enterica from different thermal
1659 environments. Evolution *55*, 33-40. 10.1554/0014-
1660 3820(2001)055[0033:EATTVE]2.0.CO;2.
1661 37. Rojas, E.R., Billings, G., Odermatt, P.D., Auer, G.K., Zhu, L., Miguel, A., Chang,
1662 F., Weibel, D.B., Theriot, J.A., and Huang, K.C. (2018). The outer membrane is
1663 an essential load-bearing element in Gram-negative bacteria. Nature *559*, 617-
1664 621. 10.1038/s41586-018-0344-3.
1665 38. Erickson, D.W., Schink, S.J., Patsalo, V., Williamson, J.R., Gerland, U., and
1666 Hwa, T. (2017). A global resource allocation strategy governs growth transition
1667 kinetics of Escherichia coli. Nature *551*, 119-123. 10.1038/nature24299.
1668 39. Knapp, B.D., Zhu, L., and Huang, K.C. (2020). SiCTeC: An inexpensive, easily
1669 assembled Peltier device for rapid temperature shifting during single-cell
1670 imaging. PLoS Biol *18*, e3000786. 10.1371/journal.pbio.3000786.
1671 40. Knapp, B.D., Odermatt, P., Rojas, E.R., Cheng, W., He, X., Huang, K.C., and
1672 Chang, F. (2019). Decoupling of Rates of Protein Synthesis from Cell Expansion
1673 Leads to Supergrowth. Cell Syst *9*, 434-445 e436. 10.1016/j.cels.2019.10.001.

1674 41. Wang, P., Robert, L., Pelletier, J., Dang, W.L., Taddei, F., Wright, A., and Jun, S.
1675 (2010). Robust growth of Escherichia coli. Curr Biol *20*, 1099-1103.
1676 10.1016/j.cub.2010.04.045.
1677 42. Schaechter, M., Maaloe, O., and Kjeldgaard, N.O. (1958). Dependency on
1678 medium and temperature of cell size and chemical composition during balanced
1679 grown of Salmonella typhimurium. J Gen Microbiol *19*, 592-606.
1680 10.1099/00221287-19-3-592.
1681 43. Maser, A., Peebo, K., Vilu, R., and Nahku, R. (2020). Amino acids are key
1682 substrates to Escherichia coli BW25113 for achieving high specific growth rate.
1683 Res Microbiol *171*, 185-193. 10.1016/j.resmic.2020.02.001.
1684 44. Cashel, M., and Gallant, J. (1969). Two compounds implicated in the function of
1685 the RC gene of Escherichia coli. Nature *221*, 838-841. 10.1038/221838a0.
1686 45. Irving, S.E., Choudhury, N.R., and Corrigan, R.M. (2021). The stringent response
1687 and physiological roles of (pp)pGpp in bacteria. Nat Rev Microbiol *19*, 256-271.
1688 10.1038/s41579-020-00470-y.
1689 46. Mackow, E.R., and Chang, F.N. (1983). Correlation between RNA synthesis and
1690 ppGpp content in Escherichia coli during temperature shifts. Mol Gen Genet *192*,
1691 5-9. 10.1007/BF00327639.
1692 47. Vadia, S., Tse, J.L., Lucena, R., Yang, Z., Kellogg, D.R., Wang, J.D., and Levin,
1693 P.A. (2017). Fatty Acid Availability Sets Cell Envelope Capacity and Dictates
1694 Microbial Cell Size. Curr Biol *27*, 1757-1767 e1755. 10.1016/j.cub.2017.05.076.
1695 48. Schink, S.J., Gough, Z., Biselli, E., Huiman, M.G., Chang, Y.F., Basan, M., and
1696 Gerland, U. (2022). MetA is a "thermal fuse" that inhibits growth and protects

1697 Escherichia coli at elevated temperatures. Cell Rep *40*, 111290.
1698 10.1016/j.celrep.2022.111290.
1699 49. Mason, C.A., Dunner, J., Indra, P., and Colangelo, T. (1999). Heat-induced
1700 expression and chemically induced expression of the Escherichia coli stress
1701 protein HtpG are affected by the growth environment. Appl Environ Microbiol *65*,
1702 3433-3440. 10.1128/AEM.65.8.3433-3440.1999.
1703 50. Ron, E.Z., and Davis, B.D. (1971). Growth rate of Escherichia coli at elevated
1704 temperatures: limitation by methionine. J Bacteriol *107*, 391-396.
1705 10.1128/jb.107.2.391-396.1971.
1706 51. Kim, S., Kim, Y., Suh, D.H., Lee, C.H., Yoo, S.M., Lee, S.Y., and Yoon, S.H.
1707 (2020). Heat-responsive and time-resolved transcriptome and metabolome
1708 analyses of Escherichia coli uncover thermo-tolerant mechanisms. Sci Rep *10*,
1709 17715. 10.1038/s41598-020-74606-8.
1710 52. Hui, S., Silverman, J.M., Chen, S.S., Erickson, D.W., Basan, M., Wang, J., Hwa,
1711 T., and Williamson, J.R. (2015). Quantitative proteomic analysis reveals a simple
1712 strategy of global resource allocation in bacteria. Mol Syst Biol *11*, 784.
1713 10.15252/msb.20145697.
1714 53. Scott, M., Gunderson, C.W., Mateescu, E.M., Zhang, Z., and Hwa, T. (2010).
1715 Interdependence of cell growth and gene expression: origins and consequences.
1716 Science *330*, 1099-1102. 10.1126/science.1192588.
1717 54. Maitra, A., and Dill, K.A. (2015). Bacterial growth laws reflect the evolutionary
1718 importance of energy efficiency. Proc Natl Acad Sci U S A *112*, 406-411.
1719 10.1073/pnas.1421138111.

1720 55. Reuveni, S., Ehrenberg, M., and Paulsson, J. (2017). Ribosomes are optimized
1721 for autocatalytic production. Nature *547*, 293-297. 10.1038/nature22998.
1722 56. Schmidt, A., Kochanowski, K., Vedelaar, S., Ahrne, E., Volkmer, B., Callipo, L.,
1723 Knoops, K., Bauer, M., Aebersold, R., and Heinemann, M. (2016). The
1724 quantitative and condition-dependent Escherichia coli proteome. Nat Biotechnol
1725 *34*, 104-110. 10.1038/nbt.3418.
1726 57. Li, G.W., Burkhardt, D., Gross, C., and Weissman, J.S. (2014). Quantifying
1727 absolute protein synthesis rates reveals principles underlying allocation of
1728 cellular resources. Cell *157*, 624-635. 10.1016/j.cell.2014.02.033.
1729 58. Galperin, M.Y., Makarova, K.S., Wolf, Y.I., and Koonin, E.V. (2015). Expanded
1730 microbial genome coverage and improved protein family annotation in the COG
1731 database. Nucleic Acids Res *43*, D261-269. 10.1093/nar/gku1223.
1732 59. Wetmore, K.M., Price, M.N., Waters, R.J., Lamson, J.S., He, J., Hoover, C.A.,
1733 Blow, M.J., Bristow, J., Butland, G., Arkin, A.P., and Deutschbauer, A. (2015).
1734 Rapid quantification of mutant fitness in diverse bacteria by sequencing randomly
1735 bar-coded transposons. mBio *6*, e00306-00315. 10.1128/mBio.00306-15.
1736 60. Cochrane, K. (2015). Elucidating ribosomes—genetic studies of the ATPase Uup
1737 and the ribosomal protein L1. (University of Michigan).
1738 61. Murina, V., Kasari, M., Takada, H., Hinnu, M., Saha, C.K., Grimshaw, J.W., Seki,
1739 T., Reith, M., Putrins, M., Tenson, T., et al. (2019). ABCF ATPases Involved in
1740 Protein Synthesis, Ribosome Assembly and Antibiotic Resistance: Structural and
1741 Functional Diversification across the Tree of Life. J Mol Biol *431*, 3568-3590.
1742 10.1016/j.jmb.2018.12.013.

1743 62. Sulavik, M.C., Houseweart, C., Cramer, C., Jiwani, N., Murgolo, N., Greene, J.,
1744 DiDomenico, B., Shaw, K.J., Miller, G.H., Hare, R., and Shimer, G. (2001).
1745 Antibiotic susceptibility profiles of Escherichia coli strains lacking multidrug efflux
1746 pump genes. Antimicrob Agents Chemother *45*, 1126-1136.
1747 10.1128/AAC.45.4.1126-1136.2001.
1748 63. Hansen, J.L., Moore, P.B., and Steitz, T.A. (2003). Structures of five antibiotics
1749 bound at the peptidyl transferase center of the large ribosomal subunit. J Mol Biol
1750 *330*, 1061-1075. 10.1016/s0022-2836(03)00668-5.
1751 64. Gao, Y.G., Selmer, M., Dunham, C.M., Weixlbaumer, A., Kelley, A.C., and
1752 Ramakrishnan, V. (2009). The structure of the ribosome with elongation factor G
1753 trapped in the posttranslocational state. Science *326*, 694-699.
1754 10.1126/science.1179709.
1755 65. Wilson, D.N. (2014). Ribosome-targeting antibiotics and mechanisms of bacterial
1756 resistance. Nat Rev Microbiol *12*, 35-48. 10.1038/nrmicro3155.
1757 66. Ikeuchi, Y., Shigi, N., Kato, J., Nishimura, A., and Suzuki, T. (2006). Mechanistic
1758 insights into sulfur relay by multiple sulfur mediators involved in thiouridine
1759 biosynthesis at tRNA wobble positions. Mol Cell *21*, 97-108.
1760 10.1016/j.molcel.2005.11.001.
1761 67. McMurry, L.M., Oethinger, M., and Levy, S.B. (1998). Triclosan targets lipid
1762 synthesis. Nature *394*, 531-532. 10.1038/28970.
1763 68. Campbell, J.W., and Cronan, J.E., Jr. (2001). Escherichia coli FadR positively
1764 regulates transcription of the fabB fatty acid biosynthetic gene. J Bacteriol *183*,
1765 5982-5990. 10.1128/JB.183.20.5982-5990.2001.

1766 69. Borgaro, J.G., Chang, A., Machutta, C.A., Zhang, X., and Tonge, P.J. (2011).
1767 Substrate recognition by beta-ketoacyl-ACP synthases. Biochemistry *50*, 10678-
1768 10686. 10.1021/bi201199x.
1769 70. Zhang, Y.M., Marrakchi, H., and Rock, C.O. (2002). The FabR (YijC)
1770 transcription factor regulates unsaturated fatty acid biosynthesis in Escherichia
1771 coli. J Biol Chem *277*, 15558-15565. 10.1074/jbc.M201399200.
1772 71. Vigh, L., Maresca, B., and Harwood, J.L. (1998). Does the membrane's physical
1773 state control the expression of heat shock and other genes? Trends Biochem Sci
1774 *23*, 369-374. 10.1016/s0968-0004(98)01279-1.
1775 72. Furusawa, C., and Kaneko, K. (2003). Zipf's law in gene expression. Phys Rev
1776 Lett *90*, 088102. 10.1103/PhysRevLett.90.088102.
1777 73. Roy, A., Goberman, D., and Pugatch, R. (2021). A unifying autocatalytic network-
1778 based framework for bacterial growth laws. Proc Natl Acad Sci U S A *118*.
1779 10.1073/pnas.2107829118.
1780 74. Sorensen, T.H., Cruys-Bagger, N., Windahl, M.S., Badino, S.F., Borch, K., and
1781 Westh, P. (2015). Temperature Effects on Kinetic Parameters and Substrate
1782 Affinity of Cel7A Cellobiohydrolases. J Biol Chem *290*, 22193-22202.
1783 10.1074/jbc.M115.658930.
1784 75. Sizer, I.W. (1943). Effects of Temperature on Enzyme Kinetics. In Advances in
1785 Enzymology and Related Areas of Molecular Biology, pp. 35-62.
1786 https://doi.org/10.1002/9780470122488.ch2.
1787 76. Ehmann, J.D., and Hultin, H.O. (1973). Temperature dependence of the
1788 Michaelis constant of chicken breast muscle lactate dehydrogenase. Journal of

1789 Food Science *38*, 1119-1121. https://doi.org/10.1111/j.1365-
1790 2621.1973.tb07216.x.
1791 77. Chang, A., Jeske, L., Ulbrich, S., Hofmann, J., Koblitz, J., Schomburg, I.,
1792 Neumann-Schaal, M., Jahn, D., and Schomburg, D. (2021). BRENDA, the
1793 ELIXIR core data resource in 2021: new developments and updates. Nucleic
1794 Acids Res *49*, D498-D508. 10.1093/nar/gkaa1025.
1795 78. Monod, J. (1949). The Growth of Bacterial Cultures. Annual Review of
1796 Microbiology *3*, 371-394. 10.1146/annurev.mi.03.100149.002103.
1797 79. Garcia-Alles, L.F., Navdaeva, V., Haenni, S., and Erni, B. (2002). The glucose-
1798 specific carrier of the Escherichia coli phosphotransferase system. Eur J
1799 Biochem *269*, 4969-4980. 10.1046/j.1432-1033.2002.03197.x.
1800 80. Bao, H., Dalal, K., Cytrynbaum, E., and Duong, F. (2015). Sequential Action of
1801 MalE and Maltose Allows Coupling ATP Hydrolysis to Translocation in the
1802 MalFGK2 Transporter. J Biol Chem *290*, 25452-25460.
1803 10.1074/jbc.M115.671826.
1804 81. Bennett, B.D., Kimball, E.H., Gao, M., Osterhout, R., Van Dien, S.J., and
1805 Rabinowitz, J.D. (2009). Absolute metabolite concentrations and implied enzyme
1806 active site occupancy in Escherichia coli. Nat Chem Biol *5*, 593-599.
1807 10.1038/nchembio.186.
1808 82. Ritchie, M.E. (2018). Reaction and diffusion thermodynamics explain optimal
1809 temperatures of biochemical reactions. Sci Rep *8*, 11105. 10.1038/s41598-018-
1810 28833-9.

1811 83. Lendenmann, U., Snozzi, M., and Egli, T. (2000). Growth kinetics of Escherichia
1812 coli with galactose and several other sugars in carbon-limited chemostat culture.
1813 Can J Microbiol *46*, 72-80. 10.1139/cjm-46-1-72.
1814 84. Meyenburg, K.V. (1971). Transport-limited growth rates in a mutant of
1815 Escherichia coli. Journal of Bacteriology *107*, 878-888. doi:10.1128/jb.107.3.878-
1816 888.1971.
1817 85. Kotte, O., Volkmer, B., Radzikowski, J.L., and Heinemann, M. (2014). Phenotypic
1818 bistability in Escherichia coli's central carbon metabolism. Mol Syst Biol *10*, 736.
1819 10.15252/msb.20135022.
1820 86. Kovarova, K., Zehnder, A.J., and Egli, T. (1996). Temperature-dependent growth
1821 kinetics of Escherichia coli ML 30 in glucose-limited continuous culture. J
1822 Bacteriol *178*, 4530-4539. 10.1128/jb.178.15.4530-4539.1996.
1823 87. Knowles, G., Downing, A.L., and Barrett, M.J. (1965). Determination of kinetic
1824 constants for nitrifying bacteria in mixed culture, with the aid of an electronic
1825 computer. J Gen Microbiol *38*, 263-278. 10.1099/00221287-38-2-263.
1826 88. Westermann, P., Ahring, B.K., and Mah, R.A. (1989). Temperature compensation
1827 in Methanosarcina barkeri by codulation of hydrogen and acetate affinity. Appl
1828 Environ Microbiol *55*, 1262-1266. 10.1128/aem.55.5.1262-1266.1989.
1829 89. Topiwala, H., and Sinclair, C.G. (1971). Temperature relationship in continous
1830 culture. Biotechnol Bioeng *13*, 795-813. 10.1002/bit.260130606.
1831 90. Kolter, R., Siegele, D.A., and Tormo, A. (1993). The stationary phase of the
1832 bacterial life cycle. Annu Rev Microbiol *47*, 855-874.
1833 10.1146/annurev.mi.47.100193.004231.

1834 91. Navarro Llorens, J.M., Tormo, A., and Martinez-Garcia, E. (2010). Stationary
1835 phase in gram-negative bacteria. FEMS Microbiol Rev *34*, 476-495.
1836 10.1111/j.1574-6976.2010.00213.x.
1837 92. Schink, S., Ammar, C., Chang, Y.F., Zimmer, R., and Basan, M. (2022). Analysis
1838 of proteome adaptation reveals a key role of the bacterial envelope in starvation
1839 survival. Mol Syst Biol *18*, e11160. 10.15252/msb.202211160.
1840 93. Jorgenson, M.A., MacCain, W.J., Meberg, B.M., Kannan, S., Bryant, J.C., and
1841 Young, K.D. (2019). Simultaneously inhibiting undecaprenyl phosphate
1842 production and peptidoglycan synthases promotes rapid lysis in Escherichia coli.
1843 Mol Microbiol *112*, 233-248. 10.1111/mmi.14265.
1844 94. Bleibtreu, A., Clermont, O., Darlu, P., Glodt, J., Branger, C., Picard, B., and
1845 Denamur, E. (2014). The rpoS gene is predominantly inactivated during
1846 laboratory storage and undergoes source-sink evolution in Escherichia coli
1847 species. J Bacteriol *196*, 4276-4284. 10.1128/JB.01972-14.
1848 95. Petersen, J., and Russell, P. (2016). Growth and the Environment of
1849 Schizosaccharomyces pombe. Cold Spring Harb Protoc *2016*, pdb top079764.
1850 10.1101/pdb.top079764.
1851 96. Wolfenden, R., Snider, M., Ridgway, C., and Miller, B. (1999). The Temperature
1852 Dependence of Enzyme Rate Enhancements. Journal of the American Chemical
1853 Society *121*, 7419-7420. 10.1021/ja991280p.
1854 97. Neidhardt, F.C., and Curtiss, R. (1996). Escherichia coli and Salmonella : cellular
1855 and molecular biology, 2nd Edition (ASM Press).

1856 98. Atolia, E., Cesar, S., Arjes, H.A., Rajendram, M., Shi, H., Knapp, B.D., Khare, S.,
1857 Aranda-Diaz, A., Lenski, R.E., and Huang, K.C. (2020). Environmental and
1858 Physiological Factors Affecting High-Throughput Measurements of Bacterial
1859 Growth. mBio *11*. 10.1128/mBio.01378-20.
1860 99. Walk, S.T., Alm, E.W., Gordon, D.M., Ram, J.L., Toranzos, G.A., Tiedje, J.M.,
1861 and Whittam, T.S. (2009). Cryptic lineages of the genus Escherichia. Appl
1862 Environ Microbiol *75*, 6534-6544. 10.1128/AEM.01262-09.
1863 100. Reas, C., and Fry, B. (2006). Processing: programming for the media arts. AI &
1864 SOCIETY *20*, 526-538. 10.1007/s00146-006-0050-9.
1865 101. Edelstein, A., Amodaj, N., Hoover, K., Vale, R., and Stuurman, N. (2010).
1866 Computer control of microscopes using microManager. Curr Protoc Mol Biol
1867 *Chapter 14*, Unit14 20. 10.1002/0471142727.mb1420s92.
1868 102. Van Valen, D.A., Kudo, T., Lane, K.M., Macklin, D.N., Quach, N.T., DeFelice,
1869 M.M., Maayan, I., Tanouchi, Y., Ashley, E.A., and Covert, M.W. (2016). Deep
1870 Learning Automates the Quantitative Analysis of Individual Cells in Live-Cell
1871 Imaging Experiments. PLoS Comput Biol *12*, e1005177.
1872 10.1371/journal.pcbi.1005177.
1873 103. Tseng, Q., Wang, I., Duchemin-Pelletier, E., Azioune, A., Carpi, N., Gao, J.,
1874 Filhol, O., Piel, M., Thery, M., and Balland, M. (2011). A new micropatterning
1875 method of soft substrates reveals that different tumorigenic signals can promote
1876 or reduce cell contraction levels. Lab Chip *11*, 2231-2240. 10.1039/c0lc00641f.
1877 104. Schindelin, J., Arganda-Carreras, I., Frise, E., Kaynig, V., Longair, M., Pietzsch,
1878 T., Preibisch, S., Rueden, C., Saalfeld, S., Schmid, B., et al. (2012). Fiji: an open-

1879 source platform for biological-image analysis. Nat Methods *9*, 676-682.
1880 10.1038/nmeth.2019.
1881 105. Ursell, T., Lee, T.K., Shiomi, D., Shi, H., Tropini, C., Monds, R.D., Colavin, A.,
1882 Billings, G., Bhaya-Grossman, I., Broxton, M., et al. (2017). Rapid, precise
1883 quantification of bacterial cellular dimensions across a genomic-scale knockout
1884 library. BMC Biol *15*, 17. 10.1186/s12915-017-0348-8.
1885 106. Traub, W.H., and Leonhard, B. (1995). Heat stability of the antimicrobial activity
1886 of sixty-two antibacterial agents. J Antimicrob Chemother *35*, 149-154.
1887 10.1093/jac/35.1.149.
1888 107. Shi, H., Hu, Y., Odermatt, P.D., Gonzalez, C.G., Zhang, L., Elias, J.E., Chang, F.,
1889 and Huang, K.C. (2021). Precise regulation of the relative rates of surface area
1890 and volume synthesis in bacterial cells growing in dynamic environments. Nat
1891 Commun *12*, 1975. 10.1038/s41467-021-22092-5.
1892 108. Karp, P.D., Paley, S., Caspi, R., Kothari, A., Krummenacker, M., Midford, P.E.,
1893 Moore, L.R., Subhraveti, P., Gama-Castro, S., Tierrafria, V.H., et al. (2023). The
1894 EcoCyc Database (2023). EcoSal Plus, eesp00022023.
1895 109. Axelrod, D., Koppel, D.E., Schlessinger, J., Elson, E., and Webb, W.W. (1976).
1896 Mobility measurement by analysis of fluorescence photobleaching recovery
1897 kinetics. Biophys J *16*, 1055-1069. 10.1016/S0006-3495(76)85755-4.
1898